Adiabatic release measurements in α-quartz between 300 and 1200 GPa: Characterization of α-quartz as a shock standard in the multimegabar regime

M. D. Knudson* and M. P. Desjarlais
Sandia National Laboratories, Albuquerque, New Mexico 87185-1195, USA
(Received 23 July 2013; revised manuscript received 2 October 2013; published 25 November 2013)

α-quartz has been used prolifically in recent years as an impedance matching standard in the multimegabar regime (1 Mbar = 100 GPa). This is due to the fact that above ∼90–100 GPa along the principal Hugoniot α-quartz becomes reflective, and thus shock velocities can be measured to high precision using velocity interferometry. This property allows for high-precision measurements, however, the accuracy of impedance matching measurements depends upon the knowledge of both the Hugoniot and the release or reshock response of α-quartz. Here, we present the results of several adiabatic release measurements of α-quartz from ∼300–1200 GPa states along the principal Hugoniot using full density polymethylpentene (commonly known as TPX), and both ∼190 and ∼110 mg/cc silica aerogel standards. These data were analyzed within the framework of a simple, analytical model that was motivated by a first-principles molecular dynamics investigation into the release response of α-quartz. Combined, this theoretical and experimental study provides a method to perform impedance matching calculations without the need to appeal to any tabular equation of state for α-quartz. As an analytical model, this method allows for propagation of all uncertainty, including the random measurement uncertainties and the systematic uncertainties of the Hugoniot and release response of α-quartz. This work establishes α-quartz for use as a high-precision standard for impedance matching in the multimegabar regime. We also note that the experimentally validated model framework should prove to be useful in the development of wide range equations of state for silica, a major constituent in the Earth's crust and mantle. Such models are crucial for accurate simulations of high-velocity giant impacts that are thought to be prevalent in the final stages of terrestrial planet formation.

DOI: 10.1103/PhysRevB.88.184107 PACS number(s): 62.50.−p, 64.30.−t

I. INTRODUCTION

The high-pressure equation of state (EOS) of materials is important for various applications ranging from, among others, planetary physics[1–3] to inertial confinement fusion (ICF).[4,5] The predominant method of obtaining EOS data in the multimegabar regime (1 Mbar = 100 GPa) is the use of shock wave compression. Paramount to this method has been the relative or impedance matching (IM) technique.[6,7] Here, the shock response of the material of interest is determined through comparison of the shock response of that material with the shock response of a known material standard.

In the past, aluminum has been the predominant IM standard in shock wave experiments. Well characterized through gas gun,[6] high-explosive,[8] explosively driven striker,[9,10] magnetically driven flyer plate,[11] and nuclear driven techniques,[12–15] the shock speed of aluminum would be used to infer the pressure state of a baseplate upon which a sample of interest was placed. Measurement of the shock speed of the sample of interest and the known response of aluminum would then allow the shocked state of the sample to be inferred. Of the methods mentioned above, only nuclear driven experiments could reach the energy densities necessary to support long duration, multimegabar shock waves, which enable large samples, accurate shock transit times, and therefore relatively precise shock wave measurements in this regime.[12–17]

With the advent of high-energy density (HED) facilities, such as large lasers or pulsed power accelerators, it is now routinely possible to reach energy densities in the laboratory capable of driving multimegabar shock waves. However, to reach the required energy densities, the volume of energy deposition is necessarily small, with sample sizes typically of order 10's–100's of microns. This results in shortened experimental durations, and subsequently less precise measurement of shock velocities in opaque materials, such as aluminum.

Because of this, α-quartz has recently become the preferred IM standard at HED facilities. Above ∼90–100 GPa along the principal Hugoniot, the locus of end states achievable through compression by large-amplitude shock waves, α-quartz melts into a conducting fluid, with appreciable reflectivity.[18–20] This enables the use of velocity interferometry [VISAR (Ref. 21)] techniques to directly measure the shock velocity to high precision. Several recent examples of the use of α-quartz as an IM standard can be found in the literature, including CO_2,[22] a glow-discharge polymer[23] (GDP), Xe,[24] H_2O,[25] He,[26] and H_2 and D_2,[27,28] which clearly show an improvement in precision with respect to previous work that utilized aluminum as the standard.

However, the accuracy of the inferred shock response of the sample of interest depends not only upon the Hugoniot response, but also the reshock or release response, depending upon the sample's relative shock impedance with respect to α-quartz. This is particularly true in the multimegabar regime, where the often used reflected Hugoniot (RH) approximation[7] breaks down due to significant entropy and temperature increases associated with large-amplitude shock waves.[29] In all of the cases referred to above, the sample impedance is less than that of α-quartz, and thus the release response is crucial to accurately infer the shock response through the IM technique.

In previous work, we accurately determined the shock response of α-quartz through numerous plate-impact, shock wave experiments on the Sandia Z machine.[19] Here, we present a detailed study of the release response of α-quartz, with the goal of characterizing the use of α-quartz as an IM standard for lower-impedance materials in the multimegabar regime. In particular, we set out to develop a simple, analytical model for IM calculations that would not require the use of a particular tabular EOS. Such a method would facilitate not only the IM calculation, but would also simplify the use of Monte Carlo methods for propagation of uncertainties in the inferred results.[24]

This goal was accomplished through both theoretical and experimental investigation of the release of α-quartz. First-principles molecular dynamics (FPMD) calculations were performed to provide insight into the release behavior. Analysis of the FPMD release calculations led to a model framework that was used as the basis to analyze a series of plate-impact, adiabatic release experiments performed at the Sandia Z machine, similar to the concept used previously to investigate the adiabatic release response of aluminum.[30] Three different low-impedance materials, full density polymethylpentene (commonly known as TPX), and both $\sim$190 and $\sim$110 mg/cc silica aerogel, were used as standards to determine release states at various pressures along the α-quartz release path. The results of these experiments validated the model framework motivated by the FPMD calculations, and provided experimentally determined parameters for the model. We note that the experimentally validated model framework should prove to be useful in the development of wide range equations of state for silica, a major constituent in the Earth's crust and mantle,[31] in that it constrains the kinematic variables of α-quartz upon release over a wide range of pressure and density. Such models are crucial for accurate simulations of high-velocity giant impacts that are thought to be prevalent in the final stages of terrestrial planet formation.[32]

As a consistency check, this analytical release model was used to perform IM calculations to infer Hugoniot states of the standards for all of the release experiments. This allowed comparison of the IM results with previous direct impact experiments used to define the standards.[33,34] In all three cases, the IM results were found to be very consistent with the direct impact results, lending confidence that the analytical release model can be used over a wide range of pressures along the Hugoniot and a wide range of shock impedances. Finally, this model was used to reanalyze recent Hugoniot experiments on GDP,[23] a candidate ablator material for ICF capsules at the National Ignition Facility, to illustrate how the model developed here differs from other methods used in the literature to perform IM with α-quartz as the standard.

Section II discusses the FPMD calculations performed to investigate the release behavior of α-quartz. Section III describes the plate-impact release experiments. The results of the experiments are discussed in Sec. IV. Section V describes the analytical release model in some detail, along with the use of the model to perform IM calculations of the release experiments and to reanalyze recent experiments on GDP. The main findings are summarized in Sec. VI.

II. FIRST-PRINCIPLES MOLECULAR DYNAMICS INVESTIGATION OF THE RELEASE RESPONSE OF α-QUARTZ

To investigate the release response of α-quartz, first-principles molecular dynamics (FPMD) calculations were performed using VASP (Vienna *ab-initio* simulation program), a plane-wave density functional theory code developed at the Technical University of Vienna.[35] We used the same method that was recently reported to be in excellent agreement with plate-impact shock wave experiments on α-quartz using the Z machine.[19] In particular, the calculated shock velocity as a function of particle velocity exhibited curvature similar to that observed experimentally in the $\sim$100–1000 GPa range, found to be the effect of disordering and dissociation of the fluid, with the maximum difference between the calculations and experiment being $\sim$0.8%. This level of agreement lends confidence in the use of this FPMD method to investigate the release response of α-quartz.

Specifically, the silicon and oxygen atoms were represented with projector augmented wave (PAW) potentials[36,37] and exchange and correlation was modeled with the Armiento-Mattsson (AM05) functionals.[38] A total of 72 atoms were included in the supercell, with a plane-wave cutoff energy of 600 eV. We note that convergence tests were run with 162 atoms and plane-wave cutoff energy of 900 eV, with markedly similar results. Simulations were performed in the canonical ensemble, with simple velocity scaling as a thermostat, and typically covered a few to several picoseconds of real time.

The release paths were calculated by taking advantage of the fact that at the initial reference state the isentrope and the Hugoniot have a second-order contact,[29] which is most easily seen by considering a Taylor series expansion of the entropy as a function of volume. Thus, for small volume changes the isentrope is well approximated by the Hugoniot. We therefore approximated each release path as a series of small Hugoniot jumps, where each calculated Hugoniot state along the approximated release path served as the initial reference state for the subsequent Hugoniot calculation. Typical volume jumps were of the order of 5%, resulting in pressure jumps of $\sim$5%–10%, with a total of $\sim$12–15 individual calculations per release path.

The Rankine-Hugoniot jump conditions,[29] which are derived by considering conservation of mass, momentum, and energy across a steady propagating wave, provide a set of equations relating the initial energy, volume, and pressure with steady-state, post-shock values:

$$(E - E_0) = (P + P_0)(V_0 - V)/2, \tag{1}$$

$$(P - P_0) = \rho_0 U_s u_p, \tag{2}$$

$$\rho = \rho_0 U_s/(U_s - u_p), \tag{3}$$

where E, P, V, ρ, U_s, and u_p denote the energy, pressure, volume, density, shock velocity, and particle velocity, respectively, and the subscript 0 denotes initial values. The first of these equations, derived from the conservation of energy, provides a prescription for calculation of the Hugoniot. For a given ρ, an initial estimate is made for the temperature T or P that would satisfy Eq. (1). A slow T ramp, typically spanning several hundred K about the estimated Hugoniot

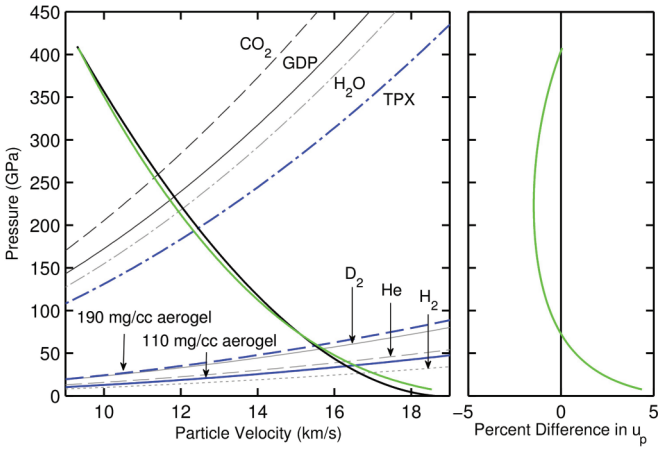

FIG. 1. (Color online) Comparison of the FPMD release path (green) to the RH (black). Also shown are the Hugoniots of CO_2 (dashed dark gray), GDP (solid dark gray), H_2O (dotted-dashed light gray), TPX (dotted-dashed blue), 190 mg/cc aerogel (dashed blue), D_2 (solid light gray), He (dashed light gray), 110 mg/cc aerogel (solid blue), and H_2 (dotted light gray). The right panel shows the particle velocity residual of the FPMD release with respect to the RH.

T, is then applied to the system at a rate of $\sim$1 K/fs. The resulting FPMD simulation allows the determination of P and E for which Eq. (1) is satisfied at the given ρ. Furthermore, the T ramp method also allows for the estimation of both $\Gamma = V(dP/dE)_V$ and the specific heat, which are very useful in estimating the T and P for the subsequent Hugoniot calculation along the approximated release path. Steady-state calculations at selected points along the release path confirmed the accuracy of the T ramp simulations in locating the Hugoniot jumps.

A release path calculated in this way from $\sim$400 GPa is shown as the green line in Fig. 1. Also shown for comparison (black line) is a reflection of the α-quartz principal Hugoniot about the particle velocity of the shocked state. This so-called reflected Hugoniot (RH) is often times used to approximate the release path in the $P - u_p$ plane.[7] At sufficiently low stress or pressure states on the principal Hugoniot, the RH approximation is reasonably good; recall that the isentrope and Hugoniot have a second-order contact. However, at higher pressures, the RH approximation breaks down, as can be seen in Fig. 1. The right panel of Fig. 1 shows a useful metric, the particle velocity residual, defined to be the percent difference in particle velocity of the FPMD release with respect to the RH. Initially, the release path drops below the RH, due to the higher sound speed at high P, however, at lower pressures the release path crosses above the RH. This is due to the fact that at a given volume, the release path has significantly higher entropy, and therefore increased thermal pressure, than the corresponding state on the RH.

For reference, shown as gray lines in Fig. 1, are Hugoniots for several materials that have recently been studied with α-quartz as a standard. As can been seen in the right panel of Fig. 1, for moderate-impedance materials, such as CO_2, GDP, and H_2O, the correction to the RH in u_p is $\sim -2\%$, while for low-impedance materials, such as D_2, He, and H_2, the correction to u_p is of similar magnitude, but opposite sign. This is significant given that errors in u_p are magnified by a factor of roughly $(\rho/\rho_0 - 1)$ when expressed in terms of ρ or density compression, i.e., $\delta\rho/\rho \sim (\rho/\rho_0 - 1)\delta u_p/u_p$, as can be seen by considering Eq. (3). These materials exhibit density compression between 3 and 4 in the multimegabar regime, and thus errors in ρ are two to three times larger than the errors in u_p.

We first chose to compare the FPMD calculated release path with that from a Mie-Grüneisen (MG) model holding Γ constant. This is an approach that has been used to determine the release path in previously reported impedance match (IM) studies that have used α-quartz as a standard.[23,28] In these studies, the reference curve for the MG model was the actual Hugoniot which shows significant curvature in the $U_s - u_p$ plane. For reasons that will become clear later on, we will refer to this model as the MG, nonlinear reference (MGNR) model. In the studies referred to above, a value for $\Gamma = 0.64$ was chosen based upon both the consideration of various EOS models for α-quartz[39] and high-P Hugoniot data for solid and porous silica.[18,40,41] The computed release path for the MGNR model with $\Gamma = 0.64$ is shown as the red line in Fig. 2. As can be seen in the figure, the MGNR model does not agree well with the calculated FPMD release path. In particular, the MGNR release path drops significantly below the FPMD release path. As can be seen in the right panel of Fig. 2, the particle velocity residual reaches a maximum of $\sim -5\%$ at $\sim$125 GPa, then abruptly increases and eventually changes sign at $\sim$50 GPa.

Better agreement with such a MGNR model can be found for larger values of Γ. The dashed red line in Fig. 2 shows the MGNR release path for $\Gamma = 1$. However, while the agreement at higher P is adequate, below $\sim$150 GPa the release path swings out to significantly higher u_p, reaching residuals of $\sim 5\%$ at $\sim$50 GPa. We note that the FPMD calculations necessary to determine the release path also allow one to infer Γ. Interestingly, the larger value of Γ necessary to improve the agreement of the MGNR model at pressures on the release

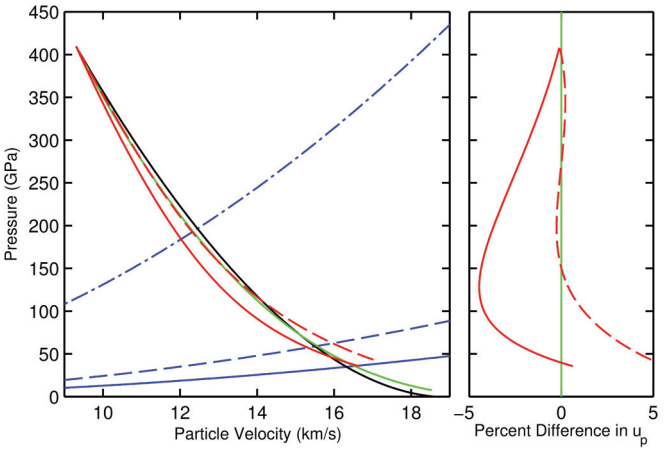

FIG. 2. (Color online) Comparison of the FPMD release path (green) with the MGNR release for $\Gamma = 0.64$ (solid red) and $\Gamma = 1$ (dashed red). Also shown for reference are the RH (black) and Hugoniots for TPX (dotted-dashed blue), 190 mg/cc aerogel (dashed blue), and 110 mg/cc aerogel (solid blue). The right panel shows the particle velocity residuals of the MGNR releases for $\Gamma = 0.64$ (solid red) and $\Gamma = 1$ (dashed red) with respect to the FPMD release.

adiabat above ∼150 GPa is in reasonable agreement with the value of Γ that is inferred from the FPMD release calculation, which is closer to unity at ∼400 GPa on the Hugoniot. This implies that the problem with the MGNR model is likely the assumption that Γ be treated as a constant along the entirety of the release path. This is not surprising given that the FPMD calculations of the Hugoniot show that the effects of disordering and dissociation of the fluid strongly influence the response of α-quartz in this regime, and one might expect that these effects may influence dP/dE in a more complicated way.

In evaluating the MG model framework, we fortuitously discovered that the FPMD release paths could be reproduced quite accurately with a very simple alteration of the model discussed above. Specifically, if one prescribes a linear $U_s - u_p$ Hugoniot response as the reference curve for the MG model, which we will call the MG, linear reference (MGLR) model, the release path can be accurately reproduced with constant Γ along nearly its entirety.

The MGLR model has two parameters: Γ and the slope S of the linear $U_s - u_p$ Hugoniot ($U_s = C_0 + Su_p$) used for the reference curve. Note that for a given value of S, there is a unique value of C_0 that will produce (P_1,u_{p1}) along the Hugoniot;

$$C_{01} = \frac{P_1}{\rho_0 u_{p1}} - S u_{p1}, \tag{4}$$

where the notation C_{01} explicitly denotes that C_0 is a function of P along the Hugoniot. The values of Γ and S can be simultaneously optimized to minimize the integral:

$$\int_{P_{\min}}^{P_1} \left[u_p^{\mathrm{rel}}(P') - u_p^{\mathrm{FPMD}}(P')\right]^2 dP', \tag{5}$$

where u_p^{rel} and u_p^{FPMD} are the particle velocities along the MGLR and FPMD release paths, respectively.

The optimal release path for the MGLR model is shown as the dashed red line in Fig. 3, with Γ = 0.356 and S = 1.198. The MGLR release path with these values of Γ and S agrees quite well with the calculated FPMD release path, as can be seen by the particle velocity residual with respect to the FPMD release path shown in the right panel of Fig. 3 (note the change in scale with respect to the right panel of Fig. 2).

Similar optimizations were performed for four other calculated FPMD release paths from various states along the principal Hugoniot ranging from ∼300–1050 GPa. The results of these optimizations are shown in Fig. 4, and the values for Γ and S are displayed in Table I. As can be seen in the figure, the MGLR model is able to reproduce quite well the FPMD release paths over the entire regime studied here. Note that the values of S obtained from the optimizations did not vary significantly over this pressure regime, nor did S change monotonically with Hugoniot pressure. This led us to consider a simplification to the model by making S a constant, thereby reducing the model to a single free parameter Γ. To do this, we considered a simultaneous minimization of the sum of integrals [Eq. (5)] for all five release paths. The results of this optimization are shown in Fig. 5 and the values of Γ and S are displayed in Table I. Comparison of Figs. 4 and 5 indicates that such a simplification in the MGLR model results in a

TABLE I. Values for Γ and S for the MGLR model for both cases (i) Γ, S optimized, and (ii) Γ optimized and S fixed.

P_H	Γ, S optimized		Γ optimized	
(GPa)	Γ	S	Γ	S
306.3	0.205	1.189	0.220	1.197
407.5	0.356	1.198	0.355	1.197
536.7	0.447	1.190	0.457	1.197
805.4	0.578	1.211	0.558	1.197
1048	0.592	1.205	0.580	1.197

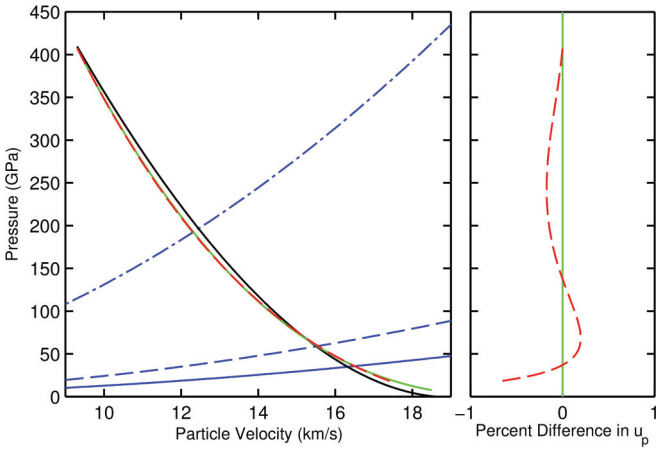

FIG. 3. (Color online) Comparison of the FPMD release path (green) with the MGLR release for Γ = 0.356 and S = 1.198 (dashed red). Also shown for reference are the RH (black) and Hugoniots for TPX (dotted-dashed blue), 190 mg/cc aerogel (dashed blue), and 110 mg/cc aerogel (solid blue). The right panel shows the particle velocity residual of the MGLR release with respect to the FPMD release (note the change in scale with respect to the right panel of Fig. 2).

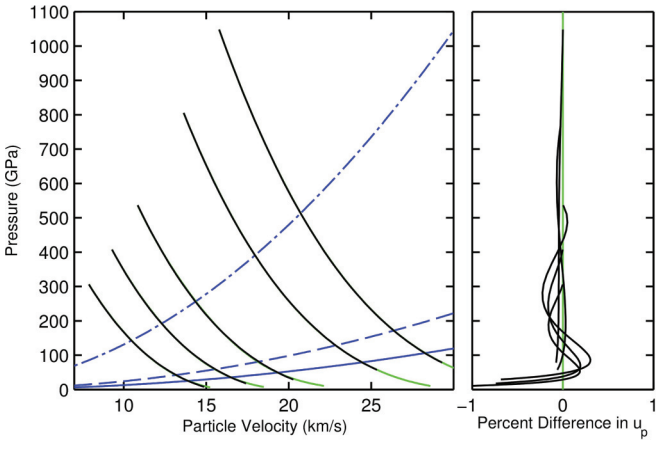

FIG. 4. (Color online) Comparison of the MGLR release paths (black) with the FPMD release paths (green) from five different principal Hugoniot states of α-quartz. Here, both Γ and S are optimized for each release path; the values are listed in Table I. Also shown for reference are the Hugoniots for TPX (dotted-dashed blue), 190 mg/cc aerogel (dashed blue), and 110 mg/cc aerogel (solid blue). The right panel shows the particle velocity residuals of the MGLR release paths with respect to the FPMD release paths.

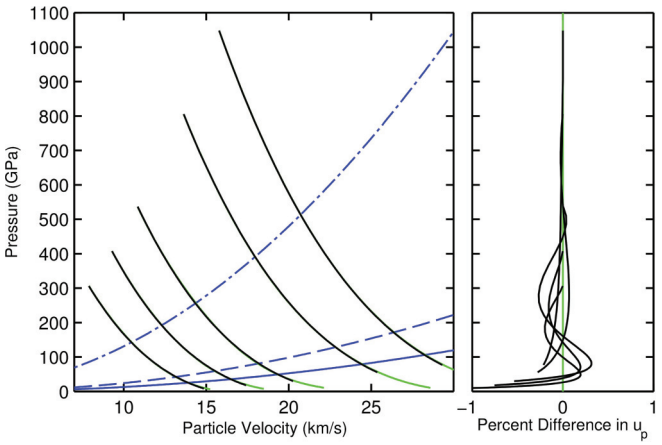

FIG. 5. (Color online) Comparison of the MGLR release paths (black) with the FPMD release paths (green) from five different principal Hugoniot states of α-quartz. Here, S is held constant at 1.197 and only Γ is optimized for each release path; the values are listed in Table I. Also shown for reference are the Hugoniots for TPX (dotted-dashed blue), 190 mg/cc aerogel (dashed blue), and 110 mg/cc aerogel (solid blue). The right panel shows the particle velocity residuals of the MGLR release paths with respect to the FPMD release paths.

negligible degradation in the agreement between the MGLR and FPMD release paths.

Unlike S, Γ was found to have a strong dependence on P. Γ is quite low at low P, increases with increasing P, and appears to saturate at a value of $\sim$0.6. This is quite close to the value of $\frac{2}{3}$ that one would expect for an ideal gas. Furthermore, the simultaneous optimization results in $S = 1.197$, which is very close to the asymptotic slope of the experimentally determined Hugoniot[19] of $S = 1.193 \pm 0.01$. While these values for Γ and S are quite intriguing, it is not clear whether these behaviors of Γ and S are the result of underlying physics, or merely a coincidence. To understand this further would require a rather extensive FPMD investigation, which is outside of the scope of this study.

It should be emphasized that the MGLR model discussed here is only intended to calculate kinematic variables for α-quartz upon release, in particular, the release paths in the $P - u_p$ plane for purposes of impedance matching. Obviously, the linear $U_s - u_p$ reference for the Hugoniot is in stark contrast to what is observed between $\sim$100 and 1000 GPa experimentally.[19] Furthermore, the rather low values of Γ that results from the MGLR model at low P are in disagreement with the estimates from the FPMD release calculations, which are closer to unity at $\sim$200–400 GPa and monotonically decrease with increasing pressure along the Hugoniot. For these reasons, it is fully expected that other aspects of the MGLR model will be incorrect. In particular, it is anticipated that the temperatures and specific heats of the MGLR model do not reflect the behavior of α-quartz in this regime. To underscore this, we choose to refer to Γ in the MGLR model as the effective Γ, or Γ_{eff}, from this point forward.

The FPMD investigation of the release response of α-quartz therefore suggests that from a given α-quartz Hugoniot state, the release path can be calculated using a MGLR model with a constant Γ_{eff}. Γ_{eff} is a function of P, or more appropriately for the purposes of an IM model, a function of U_s^{quartz} along the α-quartz Hugoniot. S of the linear $U_s - u_p$ Hugoniot used as the reference for the MG model is held fixed at $S = 1.197$. C_{01} is then determined through Eq. (4). This model serves as the framework for analysis of the release measurements that will be discussed in the next section.

III. EXPERIMENTAL α-QUARTZ RELEASE MEASUREMENTS

A series of planar, plate-impact, shock wave experiments were performed to investigate the release response of α-quartz. Three different low-impedance standards were used to obtain release states from shocked α-quartz: polymethylpentene (commonly known as TPX), and both $\sim$190 and $\sim$110 mg/cc silica aerogel. The shock response of these standards have been previously investigated on the Z machine through plate-impact, shock wave experiments.[33,34] Since these samples are solid, they could be directly impacted by the flyer plate, and thus the Hugoniot states could be inferred through simple IM with aluminum under compression, to relatively high precision. The linear $U_s - u_p$ coefficients and associated uncertainties for these three materials, which were used in the analysis of the release experiments described here, are listed in Table II.

These experiments were performed at the Sandia Z machine,[42] a pulsed power accelerator capable of generating $\sim$20 MA currents and $\sim$10 MGauss magnetic fields in a short-circuit load. The load, which is nominally 4 to 5 cm in each dimension, is designed to compress the cathode and explode the anode outward as flyer plates, producing impact velocities in excess of 30 km/s.[43,44]

Two different load geometries were used in this study. The first, referred to as a coaxial load, has anode plates completely surrounding a central rectangular cathode stalk.[43] Two of these anode plates are designed to be aluminum flyer plates with initial dimensions of approximately 40 mm in height, 20 mm in width, and 1 mm in thickness. The anode box is intentionally aligned asymmetric about the cathode stalk, with feed gaps of 1 and 1.4 mm on the two flyer plate sides. This asymmetry allows for different magnetic pressure in the two gaps, resulting in two different peak flyer plate velocities for each firing of the Z machine, thereby increasing data return.

The second load geometry, referred to as a stripline load, has a single anode plate opposite a similar cathode plate with a single 1-mm feed gap.[44] In this case, both the anode and cathode are flyer plates with initial dimensions of

TABLE II. TPX and silica aerogel $U_s - u_p$ coefficients and covariance matrix elements (Refs. 33 and 34). Note that the values for the aerogel standards are slightly different than those reported in Ref. 33 due to a more careful treatment of the uncertainty in the refractive index of the aerogel.

	C_0 (km/s)	S	$\sigma^2_{C_0}$ ($\times 10^{-3}$)	σ^2_S ($\times 10^{-3}$)	$\sigma_{C_0}\sigma_S$ ($\times 10^{-3}$)
TPX	2.707	1.307	3.485	0.0174	−0.2252
190 mg/cc aerogel	−0.385	1.248	26.31	0.271	−1.493
110 mg/cc aerogel	−0.710	1.233	44.37	0.156	−2.208

approximately 36 mm in height, 10 mm in width, and 1 mm in thickness. The benefit of this design is that a significantly larger current density is achieved with respect to the coaxial load, thereby enabling higher flyer plate velocities to be achieved. However, in this case both flyer plates reach essentially the same impact velocity and thus only a single Hugoniot point is obtained for each firing of the Z machine.

Upon discharge of the stored energy within the Marx capacitor banks, a shaped current pulse of ∼300 ns duration and ∼20 MA in magnitude is directed through the experimental load. The large current induces a large magnetic field, and the resulting $\vec{J} \times \vec{B}$ force propels the flyer plates outward. With proper load design and temporal shaping of the current pulse, accelerations of a few tens of Gg are produced that drive the solid aluminum panels across a 3–5 mm vacuum gap, ultimately reaching impact velocities of ∼12–32 km/s depending upon the load geometry and the peak charge voltage of the accelerator. More details regarding the flyer plate launch and the state of the flyer plates at impact can be found in Refs. 43 and 44.

The α-quartz (single crystal, z cut, obtained from Argus International), TPX (obtained from Mitsui Chemicals America), and ∼190 and ∼110 mg/cc silica aerogel (fabricated by General Atomics) samples were all nominally 5 mm in lateral dimension. The thickness of the α-quartz was nominally 300 μm, while the thicknesses of the release standards were all nominally 1000 μm. The samples were metrologized using a measuring microscope to determine sample diameters and an interferometer to measure thickness to a precision of ∼5 μm and less than 1 μm, respectively. Density of the silica aerogel was inferred from high-precision mass measurements and inferred volume assuming the samples were right-circular cylinders. Slight departure from the right-circular cylinder assumption resulted in density uncertainty of ∼2% and ∼5% for the 190 and 110 mg/cc aerogels, respectively.

The α-quartz samples and release standards were glued together to form experimental "stacks." A low-viscosity epoxy (Ångströmbond) was used to bond the TPX directly to the α-quartz sample. For the silica aerogel standards, a high-viscosity, UV cure epoxy was used. A high-viscosity epoxy was chosen to inhibit wicking of the epoxy into the porous aerogel samples. To further mitigate epoxy uptake, the α-quartz and aerogel samples were tacked together using four small beads of epoxy on the outer edges, thereby ensuring that the central region of the "stack" was free from epoxy. These experimental "stacks" were mounted into a target frame using the UV cure epoxy with similar gluing techniques, with the α-quartz sample facing the impact side of the target frame. The target frame was then mounted into the panel with a prescribed flight distance between 3 and 5 mm, depending upon the desired peak impact velocity (see Fig. 1 in Ref. 33).

The flyer plates and experimental "stacks" were diagnosed using a velocity interferometer [VISAR (Ref. 21)]. Since all of the materials in the "stacks" are transparent, the 532-nm laser light could pass through the "stack" and reflect off the flyer plate surface, as illustrated in the inset of Fig. 6. This allowed an in-line measurement of the flyer plate velocity from initial motion to impact. Upon impact, a several 100's of GPa shock was sent through the α-quartz sample. This shock was of sufficient magnitude that the shocked α-quartz became

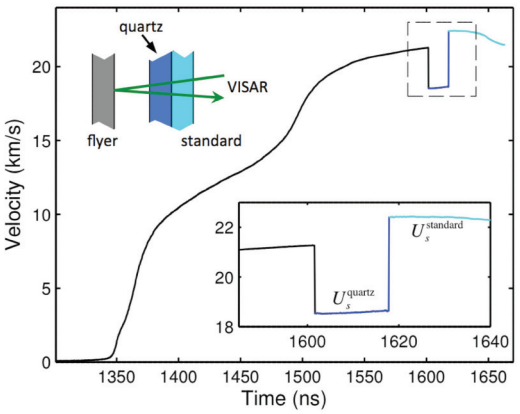

FIG. 6. (Color online) Representative experimental VISAR data. Black line, aluminum flyer plate velocity; blue (cyan) line, α-quartz (release standard) shock velocity. The inset shows a schematic of the experimental configuration. Note the dimensions are not to scale.

weakly reflective in the visible range. This immediate onset of reflectivity allowed for direct measurement of the shock velocity within the α-quartz using the VISAR diagnostic. Upon traversal of the α-quartz sample, the shock was transmitted into the release standard and a substantial release wave was reflected back into the α-quartz sample. The resulting 10 to 100's of GPa shock in the release standard was of sufficient magnitude that the release standard also became weakly reflecting, allowing direct measure of the shock velocity in the release standard with the VISAR diagnostic. Representative velocity profiles are shown in Fig. 6.

Ambiguity in the fringe shift upon both impact and transition of the shock velocity measurement from the α-quartz sample to the release standard was mitigated through the use of three different VISAR sensitivities, or velocity per fringe (vpf) settings, at each measurement location. Furthermore, integration of the shock velocity provided a trajectory of the shock through the α-quartz and release standard, which allowed for comparison of the measured α-quartz and release standard thicknesses to the inferred shock transit through each of the materials. Each measurement location included a high-sensitivity vpf setting of 0.2771 km/s/fringe. We conservatively estimate the resolution of the VISAR system at one tenth of a fringe, resulting in uncertainty in flyer plate and shock velocities of a few tenths of a percent.

A correction to the vpf was necessary to obtain the correct shock velocity in the α-quartz sample and the release standards. As the reflecting shock transits the sample, the thickness of the unshocked material through which the laser passes decreases with time, which contributes to the rate of change of the optical path. It can be shown that for this case, the apparent velocity v_a must be reduced by a factor equal to the refractive index of the unshocked material: $v = v_a/n_0$. The values of n_0 used in this study for α-quartz, TPX, and the ∼190 and ∼110 mg/cc silica aerogel were 1.547, 1.462, 1.038, and 1.02, respectively.[33,45–48] The uncertainties in n_0 for α-quartz and TPX are negligible, while the uncertainties in n_0 for both initial densities of aerogel were 1%.

The α-quartz release experiments were analyzed within the framework of the MGLR model described in the previous

TABLE III. α-quartz coefficients for the cubic $U_s - u_p$ relation $U_s^{\text{quartz}} = \sum_{n=0}^{3} a_n u_p^n$.

a_0 (km/s)	a_1	a_2 (km/s)$^{-1}$	a_3 (km/s)$^{-2}$
1.754	1.862	-3.364×10^{-2}	5.666×10^{-4}

section, which is graphically illustrated in Fig. 7. The measured U_s^{quartz} and known Hugoniot defined the initial state in the $P - u_p$ plane, (P_1, u_{p1}). For the purposes of this analysis, we used a weighted, least-squares cubic fit[49] to the α-quartz $U_s - u_p$ data of Ref. 19 along with recent data obtained using the same method (see Appendix). The fit parameters and uncertainties are listed in Tables III and IV. This functional form was used in place of the modified universal liquid Hugoniot form reported in Ref. 19 to facilitate the use of a Monte Carlo technique for error propagation. The measured shock velocity and the known Hugoniot of the release standard defined the release state (P_r, u_{pr}) along the α-quartz release path. The MGLR model, with $S = 1.197$, was then used to determine the value of Γ_{eff} such that the release path emanating from (P_1, u_{p1}) went through the point (P_r, u_{pr}).

This analysis lends itself well to a Monte Carlo method for error propagation.[24] A sequence of calculations was performed where for each series of calculations the following procedure was followed. First, the coefficients of the cubic fit to the α-quartz Hugoniot (Table III) were sampled within their uncertainty defined by the covariance matrix (Table IV) to propagate the uncertainty in the α-quartz standard. In the case of the aerogel release measurements, n_0 was sampled within its systematic uncertainty; as this is a systematic uncertainty, this value for n_0 was used for all of the subsequent direct impact and release IM calculations within this series of calculations. IM calculations were then carried out for the previous direct impact experiments,[33,34] where v_f and U_s^{standard} were sampled within their random uncertainty (in the case of the aerogel standards, each of the measured U_s^{gel} is multiplied by the factor $1.032/n_0$ or $1.02/n_0$ depending on the initial density). The resulting $U_s - u_p$ points were then used to determine a weighted, least-squares linear fit for the $U_s - u_p$ response of the standard. Next, the measured quantities U_s^{quartz} and U_s^{standard} for the release experiments described here were sampled within their random measurement uncertainties and the cubic and linear $U_s - u_p$ fits were used to determine (P_1, u_{p1}) and (P_r, u_{pr}), respectively (again, in the case of the aerogel standards, U_s^{gel} was further modified by the same n_0 that was used in the IM analysis of the direct impact experiments). Finally, the inferred quantity Γ_{eff} was determined for each release experiment in the entire data set. This process was repeated for 10^6 iterations. The reported value and one-sigma uncertainty of the inferred quantity Γ_{eff} was taken to be the mean and standard deviation of the Monte Carlo distributions, respectively. We note that because (i) n_0 for the aerogel samples is common to both the direct impact experiments and the release experiments, and (ii) the shock impedance of the aerogel is so much lower than the shock impedance of both aluminum and α-quartz, Γ_{eff} is only weakly dependent on n_0, and the 1% uncertainty does not contribute significantly to the uncertainty in Γ_{eff} (the 1% uncertainty in n_0 results in ~0.5% uncertainty in Γ_{eff}).

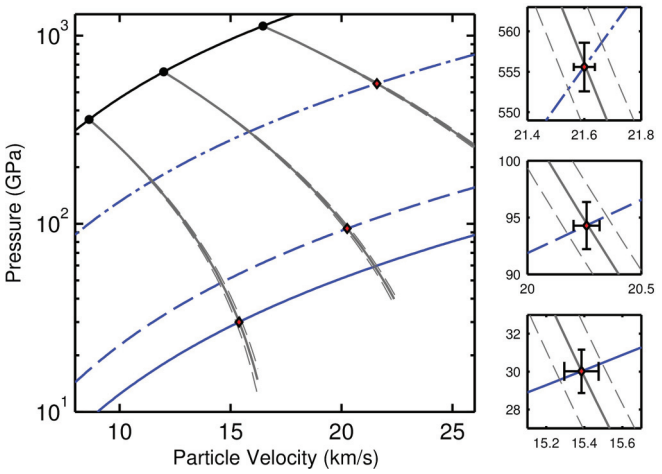

FIG. 7. (Color online) α-quartz release measurements. Black line, α-quartz principal Hugoniot; black circles, initial shocked states of α-quartz; dotted-dashed blue line, TPX Hugoniot; dashed (solid) blue line, 190 mg/cc (110 mg/cc) silica aerogel Hugoniot; red diamonds, measured release states; solid (dashed) gray lines, release paths for the best fit Γ_{eff} (one-sigma standard deviation). Right panels shown for more detail.

Uncertainties determined in this way are illustrated in Fig. 7, which show the one-sigma standard deviations of P_r and u_{pr}, and the release paths for $\Gamma_{\text{eff}} \pm \sigma_\Gamma$. Note that the uncertainty in u_{pr} that arises from both the uncertainty of the standard Hugoniot and the measured U_s^{standard} is less than 1%, and provides a tight constraint on the value of Γ_{eff} that connects (P_1, u_{p1}) and (P_r, u_{pr}). This translates into an uncertainty in Γ_{eff} of between 0.03 and 0.08 for the individual release measurements.

IV. EXPERIMENTAL RESULTS AND DISCUSSION

A total of 9, 6, and 6 α-quartz release experiments were performed with TPX, ~190 and ~110 mg/cc silica aerogel, respectively. The pertinent parameters for these experiments are listed in Tables V–VII. U_s^{quartz}, U_s^{standard}, and ρ_0^{standard} denote the measured shock velocities in the α-quartz sample and release standard, and density of the release standard, respectively. Γ_{eff} denotes the inferred value of the effective

TABLE IV. α-quartz covariance matrix elements for the cubic $U_s - u_p$ relation $U_s^{\text{quartz}} = \sum_{n=0}^{3} a_n u_p^n$.

$\sigma_{a_0}^2$ ($\times 10^{-2}$)	$\sigma_{a_0}\sigma_{a_1}$ ($\times 10^{-3}$)	$\sigma_{a_0}\sigma_{a_2}$ ($\times 10^{-4}$)	$\sigma_{a_0}\sigma_{a_3}$ ($\times 10^{-5}$)	$\sigma_{a_1}^2$ ($\times 10^{-3}$)	$\sigma_{a_1}\sigma_{a_2}$ ($\times 10^{-4}$)	$\sigma_{a_1}\sigma_{a_3}$ ($\times 10^{-6}$)	$\sigma_{a_2}^2$ ($\times 10^{-5}$)	$\sigma_{a_2}\sigma_{a_3}$ ($\times 10^{-7}$)	$\sigma_{a_3}^2$ ($\times 10^{-8}$)
2.097	−6.159	5.566	−1.572	1.877	−1.742	5.017	1.650	−4.834	1.438

TABLE V. $\Gamma_{\rm eff}$ for the TPX release experiments. $U_s^{\rm quartz}$, $U_s^{\rm TPX}$, and $\rho_0^{\rm TPX}$ are the measured shock velocities of the α-quartz and TPX samples, and the measured TPX initial density. $\Gamma_{\rm eff}$ is the inferred value of the effective Γ for the MGLR model determined as described in Sec. III. $u_p^{\rm IM}$ is the inferred particle velocity in the shocked TPX determined from the MGLR model as described in Sec. V.

Expt.	$U_s^{\rm quartz}$ (km/s)	$U_s^{\rm TPX}$ (km/s)	$\rho_0^{\rm TPX}$ (g/cc)	$\Gamma_{\rm eff}$	$u_p^{\rm IM}$ (km/s)
Z2436	15.69 ± 0.03	17.64 ± 0.03	0.83 ± 0.004	0.233 ± 0.075	11.48 ± 0.07
Z2450N	16.30 ± 0.03	18.43 ± 0.03	0.83 ± 0.004	0.340 ± 0.070	12.05 ± 0.07
Z2450S	17.45 ± 0.03	19.90 ± 0.03	0.83 ± 0.004	0.442 ± 0.061	13.17 ± 0.07
Z2345N	20.45 ± 0.03	23.79 ± 0.03	0.83 ± 0.004	0.582 ± 0.047	16.14 ± 0.08
Z2345S	21.69 ± 0.03	25.44 ± 0.03	0.83 ± 0.004	0.622 ± 0.043	17.40 ± 0.08
Z2333N	22.00 ± 0.03	25.86 ± 0.03	0.83 ± 0.004	0.631 ± 0.043	17.72 ± 0.08
Z2333S	22.97 ± 0.03	27.15 ± 0.03	0.83 ± 0.004	0.633 ± 0.040	18.71 ± 0.08
Z2375	25.19 ± 0.03	30.10 ± 0.03	0.83 ± 0.004	0.611 ± 0.034	21.02 ± 0.09
Z2332	25.82 ± 0.03	30.95 ± 0.03	0.83 ± 0.004	0.604 ± 0.033	21.68 ± 0.10

Γ for the MGLR model with $S = 1.197$, obtained using the method described in the previous section. $u_p^{\rm IM}$ is the inferred particle velocity in the shocked standard as determined through IM calculations using the MGLR model. These calculations will be discussed in the next section.

The values for $\Gamma_{\rm eff}$ inferred from all three release standards are plotted as a function of $U_s^{\rm quartz}$ in Fig. 8. Also plotted in the figure are the optimized $\Gamma_{\rm eff}$ that best match the FPMD release paths using the MGLR model with $S = 1.197$. The trend exhibited by the experimentally determined $\Gamma_{\rm eff}$ is very similar to that exhibited by the FPMD derived values. Furthermore, the data for all three release standards, which vary by roughly one order of magnitude in shock impedance, all fall along the same trend line. These two observations are a strong indicator that the MGLR framework adequately describes the release response of α-quartz in the multimegabar regime over a fairly substantial pressure range along the Hugoniot and over a wide range of shock impedances.

Just as in the case of the FPMD derived $\Gamma_{\rm eff}$, the experimentally determined $\Gamma_{\rm eff}$ appears to saturate at high P. We therefore fit the experimentally determined $\Gamma_{\rm eff}$ to a simple exponential functional form that exhibits this type of behavior:

$$\Gamma_{\rm eff} = a_1\{1 - \exp[-a_2(U_s - a_3)^{3/2}]\}. \quad (6)$$

As can be seen in Fig. 8, the weighted fit to this functional form provides a reasonably good description of the experimentally determined $\Gamma_{\rm eff}$. Also shown in the figure are the one-sigma uncertainty bands, which take into account the correlation of the uncertainty in the parameters from the weighted fit. These best-fit values of the parameters and the covariance matrix elements are listed in Table VIII.

The best-fit trend line, while exhibiting similar behavior to FPMD determined $\Gamma_{\rm eff}$, appears to be systematically larger at the highest pressures investigated in this study (above $\sim$5 Mbar). As can be seen from Fig. 2, a larger value of Γ corresponds to a larger u_p along the release path. The magnitude of the difference between the experimentally determined $\Gamma_{\rm eff}$ with that determined through the FPMD calculations is on the order of the one-sigma uncertainty bound, which is $\sim$0.02–0.04 over this pressure range. This translates to roughly 0.5% in u_p, and thus the experimentally determined $\Gamma_{\rm eff}$ suggest that the actual release paths have systematically larger u_p of $\sim$0.5% with respect to the FPMD release paths from Hugoniot states at high pressure.

We caution against the use of this model outside of the range of the experimental data. This is particularly true for $U_s^{\rm quartz}$ below $\sim$15 km/s, where there is no data and it is unclear how best to extrapolate. Because $\Gamma_{\rm eff}$ seems to be saturating at high P, one could likely use this fit for $U_s^{\rm quartz}$ above $\sim$26 km/s with some confidence. At pressures above this limit, roughly 1150 GPa, the Hugoniot asymptotes to a linear response[19] and $\Gamma_{\rm eff}$ approaches a value consistent with the actual Γ from the FPMD calculations, close to what one would expect for an ideal gas. Both of these behaviors are presumably because P is

TABLE VI. $\Gamma_{\rm eff}$ for the $\sim$190 mg/cc silica aerogel release experiments. $U_s^{\rm quartz}$, $U_s^{\rm gel}$, and $\rho_0^{\rm gel}$ are the measured shock velocities of the α-quartz and aerogel samples, and the measured aerogel initial density. $\Gamma_{\rm eff}$ is the inferred value of the effective Γ for the MGLR model determined as described in Sec. III. $u_p^{\rm IM}$ is the inferred particle velocity in the shocked aerogel determined from the MGLR model as described in Sec. V. Note that in addition to the random uncertainty in $U_s^{\rm gel}$ listed below, there is an additional 1% systematic uncertainty arising from the uncertainty in the refractive index of the aerogel.

Expt.	$U_s^{\rm quartz}$ (km/s)	$U_s^{\rm gel}$ (km/s)	$\rho_0^{\rm gel}$ (mg/cc)	$\Gamma_{\rm eff}$	$u_p^{\rm IM}$ (km/s)
Z2093N	15.27 ± 0.03	17.07 ± 0.03	190 ± 4	0.248 ± 0.045	14.01 ± 0.10
Z2093S	16.64 ± 0.03	19.20 ± 0.03	188 ± 4	0.347 ± 0.040	15.75 ± 0.10
Z2125N	18.69 ± 0.03	22.45 ± 0.03	187 ± 4	0.464 ± 0.037	18.38 ± 0.11
Z2125S	20.23 ± 0.03	24.89 ± 0.03	187 ± 4	0.503 ± 0.036	20.40 ± 0.12
Z2094N	20.89 ± 0.03	26.04 ± 0.03	185 ± 4	0.539 ± 0.037	21.29 ± 0.12
Z2094S	22.29 ± 0.03	28.28 ± 0.03	187 ± 4	0.559 ± 0.036	23.12 ± 0.13

TABLE VII. $\Gamma_{\rm eff}$ for the ~110 mg/cc silica aerogel release experiments. $U_s^{\rm quartz}$, $U_s^{\rm gel}$, and $\rho_0^{\rm gel}$ are the measured shock velocities of the α-quartz and aerogel samples, and the measured aerogel initial density. $\Gamma_{\rm eff}$ is the inferred value of the effective Γ for the MGLR model determined as described in Sec. III. $u_p^{\rm IM}$ is the inferred particle velocity in the shocked aerogel determined from the MGLR model as described in Sec. V. Note that in addition to the random uncertainty in $U_s^{\rm gel}$ listed below, there is an additional 1% systematic uncertainty arising from the uncertainty in the refractive index of the aerogel.

Expt.	$U_s^{\rm quartz}$ (km/s)	$U_s^{\rm gel}$(km/s)	$\rho_0^{\rm gel}$ (mg/cc)	$\Gamma_{\rm eff}$	$u_p^{\rm IM}$ (km/s)
Z2436	15.69 ± 0.03	18.25 ± 0.03	107 ± 6	0.326 ± 0.055	15.32 ± 0.12
Z2450N	16.31 ± 0.03	19.21 ± 0.03	105 ± 6	0.329 ± 0.052	16.20 ± 0.12
Z2450S	17.42 ± 0.03	20.99 ± 0.03	106 ± 6	0.374 ± 0.050	17.72 ± 0.13
Z2345N	20.46 ± 0.03	26.20 ± 0.03	112 ± 6	0.555 ± 0.058	21.88 ± 0.14
Z2345S	21.72 ± 0.03	28.34 ± 0.03	110 ± 6	0.552 ± 0.056	23.71 ± 0.15
Z2375	25.13 ± 0.03	34.29 ± 0.03	107 ± 6	0.549 ± 0.055	28.69 ± 0.18

sufficiently high that the effects of disordering and dissociation are becoming less important.[19,20]

V. ANALYTICAL RELEASE MODEL

In this section, we discuss in some detail exactly how one uses the MGLR model for performing IM calculations and how to incorporate the IM calculation into a Monte Carlo approach for uncertainty propagation. We then provide several examples of the use of the MGLR model. We first use the MGLR model to obtain Hugoniot states through IM for all of the α-quartz release experiments described in the previous sections. Finally, the MGLR model is used to reanalyze recent experiments on a glow-discharge polymer[23] (GDP) to illustrate the differences between the MGLR model and approaches that have been used in the literature to infer Hugoniot states with α-quartz as the standard.

Measurement of $U_s^{\rm quartz}$ determines (i) the Hugoniot state of the α-quartz, and thus (P_1, u_{p1}) from which the release path emanates, (ii) the value of C_{01} that, along with $S = 1.197$, defines the Hugoniot reference curve for the MGLR model [Eq. (4)], and (iii) the value of $\Gamma_{\rm eff}$ [Eq. (6)]. One then solves the set of equations

$$P = P_H(V; C_{01}, S) + \frac{\Gamma_{\rm eff}}{V}[E - E_H(V; C_{01}, S)], \tag{7}$$

$$d(E_s - E_0) = -P_s dV, \tag{8}$$

where P_H and E_H denote the pressure and energy of the reference Hugoniot, which are related through the Rankine-Hugoniot jump conditions [Eqs. (1)–(3)], and P_s and E_s denote the pressure and energy along the isentrope. The solution to this set of equations provides P_s:

$$P_s = P_H(V; C_{01}, S)\left[1 - \frac{\Gamma_{\rm eff}}{2}\left(\frac{V_0}{V} - 1\right)\right] + \frac{\Gamma_{\rm eff}}{V}(E_s - E_0), \tag{9}$$

where Eq. (8) is integrated using Eq. (9) to give

$$(E_s - E_0) = \frac{P_1 V_0}{2}\left(\frac{\eta - 1}{\eta}\right)\left(\frac{V_1}{V}\right)^{\Gamma_{\rm eff}} - \left(\frac{V_1}{V}\right)^{\Gamma_{\rm eff}} \int_{V_1}^{V} \left(\frac{V'}{V_1}\right)^{\Gamma_{\rm eff}} \times P_H\left[1 - \frac{\Gamma_{\rm eff}}{2}\left(\frac{V_0}{V'} - 1\right)\right] dV', \tag{10}$$

and $\eta = V_0/V_1 = \rho_1/\rho_0$ has been introduced as the compression factor. Note that for a linear $U_s - u_p$ reference Hugoniot, P_H can be written as

$$P_H = \frac{\rho_0 C_{01}^2 \left(\frac{V_0}{V} - 1\right)\left(\frac{V_0}{V}\right)}{\left[S - (S-1)\frac{V_0}{V}\right]^2}. \tag{11}$$

Given $U_s^{\rm quartz}$, which determines P_1, V_1, C_{01}, $\Gamma_{\rm eff}$, and η, Eqs. (9)–(11) then express P_s strictly as a function of V.

One can then compute u_p along the release isentrope through the Reimann integral:

$$u_p = u_{p1} + \int_{P_1}^{P} \frac{V dP_s}{C_s}, \tag{12}$$

where the sound speed along the release isentrope C_s is given by

$$C_s^2 = -V^2 \left.\frac{\partial P_s}{\partial V}\right|_S. \tag{13}$$

Finally, $P_1^{\rm sample}$ and $u_{p1}^{\rm sample}$ in the shocked state of the sample material are determined by the intersection of (P, u_p) along the release path and the chord $P = \rho_0^{\rm sample} U_s^{\rm sample} u_p$ [see Eq. (2)].

This IM model lends itself well to a Monte Carlo method for uncertainty propagation.[24] For each series of IM calculations, the coefficients of the cubic fit to the α-quartz Hugoniot (Table III) are sampled within their uncertainty defined by the covariance matrix (Table IV). This propagates the uncertainty

TABLE VIII. Fit parameters and covariance matrix elements for $\Gamma_{\rm eff}(U_s)$.

a_1	a_2 $({\rm km/s})^{-2/3}$	a_3 (km/s)	$\sigma_{a_1}^2$ $(\times 10^{-4})$	$\sigma_{a_1}\sigma_{a_2}$ $(\times 10^{-4})$	$\sigma_{a_1}\sigma_{a_3}$ $(\times 10^{-3})$	$\sigma_{a_2}^2$ $(\times 10^{-4})$	$\sigma_{a_2}\sigma_{a_3}$ $(\times 10^{-2})$	$\sigma_{a_3}^2$ $(\times 10^{-1})$
0.619	0.0882	12.0922	4.357	−3.935	−9.324	5.039	1.370	4.103

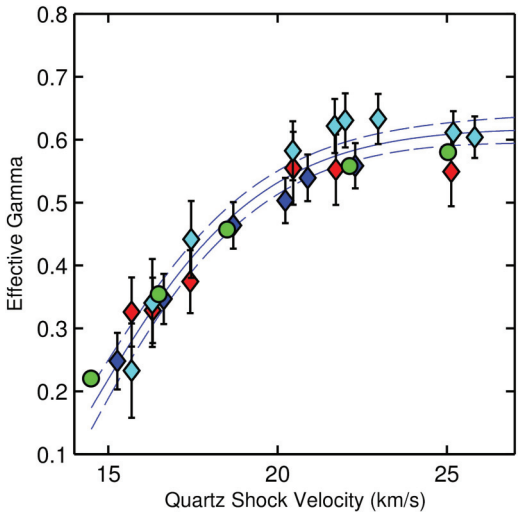

FIG. 8. (Color online) $\Gamma_{\rm eff}$ as a function of $U_s^{\rm quartz}$. Cyan diamonds, TPX release measurements; blue (red) diamonds, ~190 (~110) mg/cc silica aerogel release measurements; green circles, FPMD release calculations; blue solid (dashed) line, best fit (one sigma deviation) to the experimental data.

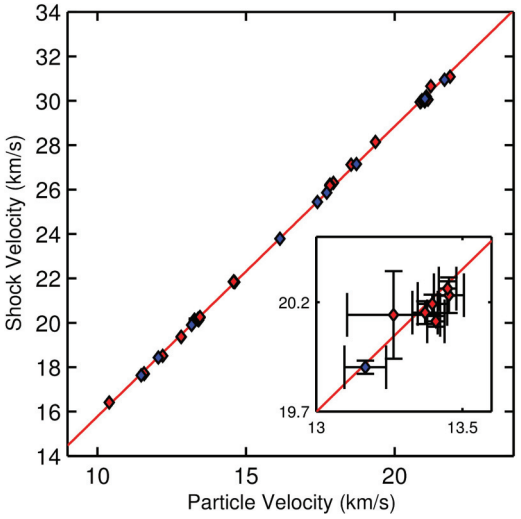

FIG. 9. (Color online) IM $U_s - u_p$ Hugoniot data (blue diamonds) compared to direct impact Hugoniot data (Ref. 34) (red diamonds) for TPX. Red line indicates the linear Hugoniot determined from a weighted, least-squares linear fit of the direct impact data. Inset shown for more detail.

in the initial state (P_1,u_{p1}) as well as the uncertainties in V_1, C_{01}, and η. Then, for each IM calculation in the series of measurements, $\Gamma_{\rm eff}$, $U_s^{\rm sample}$, and $\rho_0^{\rm sample}$ are all sampled with their one-sigma uncertainty. $(P_1^{\rm sample},u_{p1}^{\rm sample})$ is then determined as the intersection of the chord and release path, and the remaining kinematic variables can be evaluated through the use of the Rankine-Hugoniot jump conditions [Eqs. (1)–(3)]. This process is repeated for 10^6 iterations, and the reported values and one-sigma uncertainties of the inferred quantities are taken to be the mean and standard deviations of the Monte Carlo distributions, respectively.

As examples of this analytical release model, and as a consistency check, this IM method was used to determine the shocked states of the release standards for all of the α-quartz release measurements listed in Tables V–VII. The results of these analyses are listed in the last column of Tables V–VII, and shown graphically as the blue symbols in Figs. 9–11. Also shown in these figures as red symbols are the direct impact data used to define the shock response of the standards.[33,34]

Two observations can be made from these comparisons. First, the resulting $U_s - u_p$ points from the IM method using the analytical release model are in excellent agreement with the direct impact results. This provides a consistency check and indicates that the assumptions of the analytical model, namely, that $\Gamma_{\rm eff}$ can be treated as a constant regardless of the impedance of the unknown material, is justified. Second, the uncertainties in the inferred u_p for both the analytical IM release model and for the direct impact experiments are comparable. At first this might seem counterintuitive in that the analytical model requires knowledge of both the Hugoniot and release of α-quartz, and thus the uncertainty should be significantly larger than the uncertainties in the direct impact experiments. However, given the high precision in which $U_s^{\rm quartz}$ can be measured and the highly constrained α-quartz Hugoniot,[19] the uncertainty in u_p of the shocked state of the α-quartz is roughly equivalent to the uncertainty in the impact velocity of the direct impact experiments. Furthermore, the set of release experiments described here characterize the release response of α-quartz as precisely, if not better, than the high-P Hugoniot of aluminum. Thus, there is essentially no loss in precision or accuracy in using the analytical IM model. This comparison illustrates the fact that α-quartz has become the most well-studied material in the multimegabar regime.

As a final example, we discuss recent Hugoniot experiments by Barrios *et al.*[23] on GDP, a candidate ablator material for inertial confinement fusion (ICF) capsules. This example illustrates the effect of both the α-quartz Hugoniot and the α-quartz release on inferred shock states when using α-quartz as an IM standard. In their study, Barrios *et al.*[23] used an

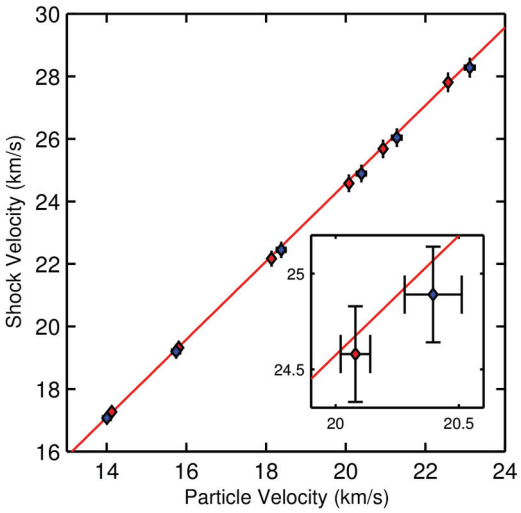

FIG. 10. (Color online) IM $U_s - u_p$ Hugoniot data (blue diamonds) compared to direct impact Hugoniot data (Ref. 33) (red diamonds) for ~190 mg/cc silica aerogel. Red line indicates the linear Hugoniot determined from a weighted, least-squares linear fit of the direct impact data. Inset shown for more detail.

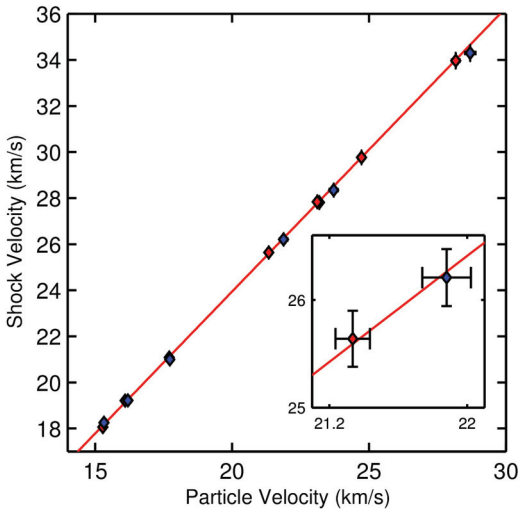

FIG. 11. (Color online) IM $U_s - u_p$ Hugoniot data (blue diamonds) compared to direct impact Hugoniot data (Ref. 33) (red diamonds) for ∼110 mg/cc silica aerogel. Red line indicates the linear Hugoniot determined from a weighted, least-squares linear fit of the direct impact data. Inset shown for more detail.

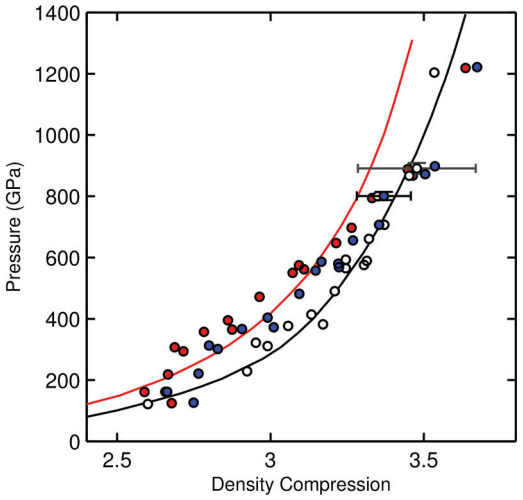

FIG. 12. (Color online) P, density compression Hugoniot for GDP. Black line, LEOS-5350 (Ref. 23); red line, Hamel model (Ref. 50). Data: open circles, Barrios *et al.* (Ref. 23); red circles, Hamel *et al.* reanalysis (Ref. 50); blue circles, this reanalysis. Gray and black error bars show representative uncertainties for the analysis of Barrios *et al.* and the present reanalysis, respectively.

α-quartz Hugoniot derived from the laser-driven data of Hicks *et al.*,[18] and a MGNR release model with a constant $\Gamma = 0.64$. Later, Hamel *et al.*[50] revisited these results using the α-quartz Hugoniot from Knudson and Desjarlais,[19] but with the same MGNR release model as that used by Barrios *et al.* Finally, we reanalyze the results using the α-quartz Hugoniot from Ref. 19, and the MGLR release model developed in this work.

A comparison of these three analyses is shown in Fig. 12 and the results are tabulated in Table IX. Comparison of the analyses of Refs. 23 and 50 show that, consistent with the conclusions of Knudson and Desjarlais in Ref. 19, the stiffer α-quartz Hugoniot leads to a stiffer inferred response of the GDP (the inferred u_p is lower for a given U_s, leading to a lower inferred ρ). Comparison of our analysis and that of Ref. 50 illustrates that the use of the MGLR release model leads to a softer response with respect to the MGNR release model (the inferred u_p is larger for a given U_s, leading to a higher inferred ρ).

Note that at P above ∼700 GPa in the GDP, which corresponds to drive P at or above ∼1000 GPa in the α-quartz, all three analyses lead to essentially the same result. This is due to the fact that (i) above ∼1000 GPa the α-quartz Hugoniots of Refs. 18 and 19 more or less converge to the asymptotic

TABLE IX. Comparison of the inferred P and ρ/ρ_0 for recent experiments on GDP using three different IM methods described in the text.

	Barrios *et al.* (Ref. 23)		Hamel *et al.* (Ref. 50)		This reanalysis	
Shot	P (GPa)	ρ/ρ_0	P (GPa)	ρ/ρ_0	P (GPa)	ρ/ρ_0
55782	122 ± 4	2.60 ± 0.14	125	2.68	127 ± 5	2.75 ± 0.09
55783	162 ± 4	2.66 ± 0.14	161	2.59	162 ± 6	2.66 ± 0.08
55781	229 ± 4	2.92 ± 0.11	218	2.67	222 ± 9	2.77 ± 0.08
55780	311 ± 5	2.99 ± 0.11	307	2.69	301 ± 11	2.83 ± 0.08
55785	322 ± 6	2.95 ± 0.10	294	2.72	313 ± 12	2.80 ± 0.08
55779	377 ± 6	3.06 ± 0.12	358	2.78	367 ± 14	2.91 ± 0.09
55784	382 ± 7	3.17 ± 0.13	365	2.88	373 ± 14	3.01 ± 0.10
55778	414 ± 7	3.13 ± 0.12	395	2.86	404 ± 15	2.99 ± 0.09
55777	490 ± 9	3.21 ± 0.14	472	2.96	481 ± 18	3.09 ± 0.10
52635	565 ± 9	3.25 ± 0.12	550	3.07	558 ± 9	3.15 ± 0.07
55774	576 ± 11	3.30 ± 0.16	562	3.11	568 ± 21	3.22 ± 0.13
55775	589 ± 11	3.31 ± 0.15	575	3.13	580 ± 5	3.22 ± 0.07
54127	593 ± 11	3.25 ± 0.16	580	3.08	586 ± 12	3.17 ± 0.11
54187	661 ± 11	3.32 ± 0.14	648	3.21	656 ± 11	3.27 ± 0.08
57164	707 ± 13	3.37 ± 0.16	697	3.26	707 ± 26	3.35 ± 0.12
57126	800 ± 14	3.35 ± 0.15	794	3.33	801 ± 13	3.37 ± 0.09
54185	867 ± 16	3.45 ± 0.16	868	3.46	872 ± 14	3.50 ± 0.09
57162	891 ± 18	3.48 ± 0.19	888	3.45	898 ± 8	3.54 ± 0.07
57163	1204 ± 27	3.53 ± 0.21	1219	3.64	1222 ± 10	3.67 ± 0.07

linear $U_s - u_p$ reported in Ref. 19, and (ii) above ~1000 GPa Γ_{eff} is approaching a value of ~0.62, which is very close to $\Gamma = 0.64$ used in the MGNR release model analyses of both Refs. 23 and 50, and roughly what one would infer for Γ from the FPMD calculations along the α-quartz Hugoniot in this regime. Based upon the discussion surrounding Fig. 2 it is expected that both the MGNR and MGLR models with the actual Γ would reproduce reasonably well the α-quartz release response in this pressure regime, particularly for a moderate impedance material such as GDP. At P below ~700 GPa in the GDP, which corresponds to the regime that is the most relevant for ICF applications,[50] these three analyses differ substantially. This is the result of the rather significant differences between the reference Hugoniots and Γ_{eff} in this regime, presumably due to the strong effects of disordering and dissociation in the fluid silica.[19,20]

Finally, and perhaps more significantly, the comparison of the three analyses displayed in Fig. 12 demonstrates that the uncertainty in the inferred shock state is significantly smaller for the MGLR analysis as compared to the MGNR analysis. This is due to the significant reduction in the uncertainty of Γ_{eff}. With no direct experimental guidance, Barrios *et al.* were forced to resort to examination of various EOS models and high-P Hugoniot data on solid and porous silica in an attempt to constrain Γ, with a resultantly large uncertainty of ± 0.11. The experiments described in Sec. III enabled a determination of Γ_{eff} with an uncertainty roughly three to five times smaller. As a result, the inferred quantities, particularly ρ, exhibit significantly lower uncertainty, thereby increasing the precision of the IM method with α-quartz as the standard.

VI. CONCLUSION

The release response of α-quartz was investigated within the framework of first-principles molecular dynamics (FPMD). These calculations provided insight into the release response, and motivated a simple Mie-Grüneisen model with a linear $U_s - u_p$ Hugoniot as the reference, referred to as the MGLR model. This model was shown to reproduce the FPMD release paths extremely well with a constant $S = 1.197$ and a constant Γ_{eff} along the release path, with Γ_{eff} being a function of U_s^{quartz}.

A series of plate-impact, shock wave experiments were performed on the Sandia Z machine to obtain adiabatic release data for α-quartz from ~300–1200 GPa states on the principal Hugoniot. Three different low-impedance standards were used, TPX, ~190 and ~110 mg/cc silica aerogel, which vary in shock impedance by roughly one order of magnitude. These data validated the MGLR model that was motivated by the FPMD study, and provided an experimentally determined Γ_{eff} as a function of U_s^{quartz}.

This theoretical and experimental study of the release response of α-quartz provides a simple, analytical model for performing IM calculations without the need to appeal to any particular tabular equation of state for α-quartz. Since the model is analytical, it is well suited for the use of Monte Carlo analysis methods, enabling all uncertainties, including the random measurement uncertainties and the systematic uncertainties in the Hugoniot and release response of α-quartz, to be propagated to the inferred quantities. We also note that the experimentally validated model framework should prove to be useful in the development of wide range equations of state for silica, a major constituent in the Earth's crust and mantle, in that it constrains the kinematic variables of α-quartz upon release over a wide range of P and ρ. Such models are crucial for accurate simulations of high-velocity giant impacts that are thought to be prevalent in the final stages of terrestrial planet formation.

It is emphasized that the MGLR model discussed here is only intended to calculate kinematic variables for α-quartz upon release, in particular, the release paths in the $P - u_p$ plane for purposes of impedance matching. Obviously, the linear $U_s - u_p$ reference for the Hugoniot in this P regime is in stark contrast to what is observed experimentally. Furthermore, the rather low values of Γ_{eff} that result from the MGLR model at low P are in disagreement with the estimates from the FPMD release calculations, which are closer to unity at ~200–400 GPa and monotonically decrease with increasing pressure along the Hugoniot. For these reasons, it is fully expected that other aspects of the MGLR model will be incorrect. In particular, it is anticipated that the temperatures and specific heats of the MGLR model do not reflect the behavior of α-quartz in this regime.

Finally, we caution against the use of this model outside of the range of the experimental data. This is particularly true for U_s^{quartz} below ~15 km/s, where there are no data and it is unclear how best to extrapolate. Because Γ_{eff} seems to be saturating at high P, one could likely use this fit for U_s^{quartz} above ~26 km/s with some confidence. At pressures above this limit, roughly 1150 GPa, the Hugoniot asymptotes to a linear response and Γ_{eff} approaches a value of $\Gamma_{\text{eff}} = 0.62$ consistent with the actual Γ from the FPMD calculations, and close to what one would expect for an ideal gas. Both of these behaviors are presumably because P is sufficiently high that the effects of disordering and dissociation in the shocked fluid are becoming less important.

As an example of its use, the MGLR model was used to infer Hugoniot states through the IM method for all of the α-quartz release measurements performed in this study. This provided a consistency check in that the IM results could be compared to the direct impact Hugoniot measurements of the standards. The Hugoniot response inferred using the analytical IM model was found to be in excellent agreement with the direct impact Hugoniot results, suggesting that the IM method can confidently be used to obtain high-precision Hugoniot measurements regardless of the shock impedance of the unknown material. Furthermore, the uncertainties in the inferred u_p for both the analytical IM release model and for the direct impact experiments were found to be comparable, indicating that there is essentially no loss in accuracy in using the analytical IM model. This comparison illustrates the fact that α-quartz has become the most well-studied material in the multimegabar regime and the standard of choice for multimegabar experiments.

ACKNOWLEDGMENTS

The authors would like to thank the large team at Sandia that contributed to the design and fabrication of the flyer plate loads and the fielding of the shock diagnostics. Sandia National

Laboratories is a multiprogram laboratory managed and operated by Sandia Corporation, a wholly owned subsidiary of Lockheed Martin Corporation, for the U.S. Department of Energy National Nuclear Security Administration under Contract No. DE-AC04-94AL85000.

APPENDIX: α-QUARTZ HUGONIOT DATA

Table X lists the $U_s - u_p$ Hugoniot data for α-quartz used to perform the weighted, least-squares cubic fit, the results of which are listed in Tables III and IV. These data are from Ref. 19 and more recent experiments performed using the same method as that described in Ref. 19. The linear $U_s - u_p$ relations for the aluminum[6,9–12,14,15,51–55] and copper[6,12,51,53,55–58] impactors used to perform the IM analysis of these direct impact experiments are listed in Table XI along with the covariance matrix elements. Note that the Hugoniot for the impactors is described by piecewise linear fits due to different slopes corresponding to the solid and liquid branches of the Hugoniot.

For comparison with Ref. 19, Tables XII and XIII lists the best-fit values and the covariance matrix elements for a weighted fit of the data listed in Table X to the functional form:

$$U_s = a + bu_p - cu_p e^{-du_p}. \quad \text{(A1)}$$

TABLE X. $U_s - u_p$ Hugoniot data for α-quartz from Ref. 19 and more recent data obtained using the same method. The impactor material is listed in the flyer column, with "Al" and "Cu" designating aluminum and copper, respectively. v_f and U_s^{quartz} are the measured flyer plate and quartz shock velocity, respectively. u_p^{quartz}, P, and ρ are the inferred quartz particle velocity, pressure, and density in the shocked state, respectively. $\sigma_{U_s}^2$, $\sigma_{u_p}^2$, and $\sigma_{U_s}\sigma_{u_p}$ are the covariance matrix elements that describe the correlation between the uncertainties in U_s and u_p.

Expt.	Flyer	v_f (km/s)	U_s^{quartz} (km/s)	u_p^{quartz} (km/s)	$\sigma_{U_s}^2$ ($\times 10^{-3}$)	$\sigma_{u_p}^2$ ($\times 10^{-3}$)	$\sigma_{U_s}\sigma_{u_p}$ ($\times 10^{-4}$)	P (GPa)	ρ (g/cc)
Z1707	Al	7.44 ± 0.05	8.65	4.02	1.600	1.065	−2.807	92.1 ± 0.8	4.95 ± 0.04
Z1707	Al	7.46 ± 0.05	8.71	4.02	1.600	1.054	−2.747	92.8 ± 0.8	4.93 ± 0.04
Z1707	Al	7.48 ± 0.05	8.75	4.03	1.600	1.057	−2.756	93.4 ± 0.8	4.91 ± 0.04
Z2378	Cu	6.08 ± 0.05	9.25	4.30	1.600	1.508	−1.722	105.3 ± 1.0	4.95 ± 0.05
Z1707	Al	8.60 ± 0.05	9.69	4.57	1.600	1.063	−2.832	117.4 ± 0.9	5.02 ± 0.04
Z1707	Al	8.65 ± 0.05	9.72	4.60	1.600	1.069	−2.809	118.4 ± 0.9	5.03 ± 0.04
Z2379	Cu	6.75 ± 0.05	9.92	4.74	1.600	1.534	−1.753	124.6 ± 1.1	5.08 ± 0.04
Z1685	Al	10.88 ± 0.05	11.41	5.70	1.600	1.112	−2.899	172.4 ± 1.1	5.30 ± 0.04
Z1685	Al	11.01 ± 0.05	11.46	5.77	1.600	1.122	−2.948	175.4 ± 1.1	5.34 ± 0.04
Z1685	Al	10.92 ± 0.05	11.47	5.72	1.600	1.114	−2.942	173.8 ± 1.1	5.28 ± 0.04
Z2055	Cu	8.53 ± 0.05	11.65	5.92	1.600	1.555	−1.889	182.7 ± 1.3	5.39 ± 0.04
Z2193	Cu	8.65 ± 0.05	11.76	6.00	1.600	1.567	−1.872	187.0 ± 1.3	5.41 ± 0.04
Z1685	Al	12.16 ± 0.05	12.37	6.33	1.600	1.142	−2.991	207.7 ± 1.2	5.43 ± 0.04
Z1685	Al	12.21 ± 0.05	12.40	6.36	1.600	1.145	−3.009	209.0 ± 1.2	5.44 ± 0.04
Z1657	Cu	9.56 ± 0.08	12.77	6.58	2.500	3.902	−2.901	222.8 ± 2.2	5.47 ± 0.06
Z1657	Cu	9.58 ± 0.08	12.82	6.59	2.500	3.937	−2.987	224.0 ± 2.2	5.45 ± 0.06
Z1681	Cu	9.71 ± 0.08	12.92	6.68	2.500	3.919	−2.768	228.6 ± 2.3	5.49 ± 0.06
Z1681	Cu	9.81 ± 0.08	12.98	6.75	2.500	3.937	−3.121	232.1 ± 2.3	5.52 ± 0.06
Z2193	Cu	9.85 ± 0.05	13.05	6.77	1.600	1.598	−1.928	234.1 ± 1.5	5.51 ± 0.04
Z2096	Cu	9.98 ± 0.05	13.16	6.86	1.600	1.615	−1.945	239.2 ± 1.5	5.54 ± 0.04
Z2262	Cu	10.00 ± 0.05	13.18	6.87	1.600	1.606	−1.949	240.0 ± 1.5	5.54 ± 0.04
Z1657	Cu	10.72 ± 0.08	13.91	7.34	2.500	3.990	−2.883	270.5 ± 2.5	5.61 ± 0.06
Z1708	Cu	10.78 ± 0.05	13.92	7.39	1.600	1.626	−1.913	272.4 ± 1.6	5.65 ± 0.04
Z1708	Cu	10.78 ± 0.05	13.95	7.38	1.600	1.616	−1.884	272.9 ± 1.6	5.63 ± 0.04
Z1681	Cu	10.89 ± 0.08	14.00	7.46	2.500	3.992	−3.031	276.8 ± 2.5	5.68 ± 0.06
Z1657	Cu	10.77 ± 0.08	14.01	7.37	2.500	3.976	−2.939	273.5 ± 2.5	5.59 ± 0.06
Z1681	Cu	11.04 ± 0.08	14.15	7.56	2.500	4.000	−3.211	283.4 ± 2.5	5.69 ± 0.06
Z1624	Cu	11.32 ± 0.08	14.37	7.74	2.500	4.004	−2.876	294.8 ± 2.6	5.75 ± 0.06
Z1624	Cu	11.31 ± 0.08	14.37	7.75	2.500	4.013	−3.014	295.0 ± 2.6	5.75 ± 0.06
Z2186	Cu	11.35 ± 0.05	14.38	7.77	1.600	1.658	−1.990	296.1 ± 1.7	5.77 ± 0.04
Z2186	Cu	11.48 ± 0.05	14.55	7.85	1.600	1.654	−1.910	302.7 ± 1.7	5.76 ± 0.04
Z1602	Cu	11.98 ± 0.08	14.96	8.19	2.500	4.023	−3.039	324.5 ± 2.7	5.85 ± 0.06
Z2093	Al	15.90 ± 0.05	14.98	8.17	1.600	1.355	−3.264	324.2 ± 1.5	5.83 ± 0.04
Z1602	Cu	12.04 ± 0.08	15.08	8.22	2.500	4.078	−3.145	328.4 ± 2.7	5.82 ± 0.06
Z1708	Cu	11.94 ± 0.05	15.10	8.14	1.600	1.706	−1.924	325.6 ± 1.8	5.75 ± 0.04
Z1708	Cu	12.02 ± 0.05	15.15	8.19	1.600	1.691	−2.071	329.0 ± 1.8	5.77 ± 0.04
Z2093	Al	16.37 ± 0.05	15.26	8.41	1.600	1.352	−3.250	339.9 ± 1.6	5.90 ± 0.04
Z2186	Cu	12.42 ± 0.05	15.45	8.47	1.600	1.734	−2.017	346.6 ± 1.9	5.86 ± 0.04
Z2186	Cu	12.54 ± 0.05	15.48	8.56	1.600	1.722	−1.959	351.0 ± 1.9	5.92 ± 0.04

TABLE X. (*Continued.*)

Expt.	Flyer	v_f (km/s)	U_s^{quartz} (km/s)	u_p^{quartz} (km/s)	$\sigma_{U_s}^2$ ($\times 10^{-3}$)	$\sigma_{u_p}^2$ ($\times 10^{-3}$)	$\sigma_{U_s}\sigma_{u_p}$ ($\times 10^{-4}$)	P (GPa)	ρ (g/cc)
Z2436	Al	16.80 ± 0.05	15.55	8.62	1.600	1.323	−3.267	355.1 ± 1.6	5.94 ± 0.04
Z1624	Cu	12.66 ± 0.08	15.57	8.64	2.500	4.090	−3.102	356.4 ± 2.8	5.95 ± 0.06
Z1624	Cu	12.67 ± 0.08	15.71	8.63	2.500	4.101	−3.166	359.2 ± 2.8	5.88 ± 0.06
Z1602	Cu	12.90 ± 0.08	15.80	8.79	2.500	4.109	−3.212	368.2 ± 2.8	5.98 ± 0.06
Z1741	Cu	12.91 ± 0.05	15.80	8.80	1.600	1.764	−2.067	368.5 ± 1.9	5.98 ± 0.04
Z1602	Cu	12.96 ± 0.08	15.94	8.82	2.500	4.070	−3.132	372.7 ± 2.9	5.94 ± 0.06
Z2476	Al	17.64 ± 0.05	16.08	9.04	1.600	1.305	−3.391	385.0 ± 1.6	6.05 ± 0.04
Z2476	Al	17.70 ± 0.05	16.16	9.06	1.600	1.305	−3.315	387.8 ± 1.7	6.03 ± 0.04
Z1741	Cu	13.30 ± 0.05	16.20	9.05	1.600	1.761	−2.054	388.7 ± 2.0	6.01 ± 0.04
Z1738	Cu	13.78 ± 0.05	16.58	9.42	1.600	1.278	−3.300	414.0 ± 1.7	6.14 ± 0.04
Z2093	Al	18.42 ± 0.05	16.58	9.37	1.600	1.597	−2.091	411.9 ± 2.0	6.10 ± 0.04
Z2114	Al	18.32 ± 0.05	16.67	9.34	1.600	1.281	−3.282	412.6 ± 1.7	6.03 ± 0.04
Z1741	Cu	13.80 ± 0.05	16.68	9.38	1.600	1.582	−1.929	414.6 ± 2.0	6.05 ± 0.04
Z1738	Cu	13.84 ± 0.05	16.73	9.29	1.600	1.590	−2.053	412.1 ± 2.0	5.96 ± 0.04
Z1918	Cu	13.70 ± 0.05	16.73	9.40	1.600	1.586	−2.036	416.9 ± 2.0	6.05 ± 0.04
Z1918	Cu	13.80 ± 0.05	16.78	9.36	1.600	1.590	−2.074	416.5 ± 2.0	6.00 ± 0.04
Z1741	Cu	13.94 ± 0.05	16.86	9.46	1.600	1.277	−3.276	422.6 ± 1.7	6.03 ± 0.04
Z2024	Al	18.57 ± 0.05	16.86	9.46	1.600	1.588	−2.099	422.8 ± 2.0	6.04 ± 0.04
Z2187	Cu	14.45 ± 0.05	17.26	9.80	1.600	1.597	−2.129	448.5 ± 2.0	6.13 ± 0.04
Z2187	Cu	14.52 ± 0.05	17.27	9.86	1.600	1.584	−2.054	451.1 ± 2.0	6.17 ± 0.04
Z1987	Al	19.27 ± 0.05	17.28	9.81	1.600	1.283	−3.356	449.3 ± 1.8	6.13 ± 0.04
Z2386	Al	19.46 ± 0.05	17.35	9.91	1.600	1.284	−3.376	455.9 ± 1.8	6.18 ± 0.04
Z2386	Al	19.50 ± 0.05	17.38	9.93	1.600	1.268	−3.398	457.6 ± 1.8	6.18 ± 0.04
Z1971	Al	19.55 ± 0.05	17.47	9.95	1.600	1.266	−3.490	460.6 ± 1.8	6.15 ± 0.04
Z2476	Al	19.58 ± 0.05	17.48	9.96	1.600	1.267	−3.336	461.6 ± 1.8	6.16 ± 0.04
Z1971	Al	19.64 ± 0.05	17.49	10.00	1.600	1.275	−3.367	463.5 ± 1.8	6.19 ± 0.04
Z1738	Cu	14.74 ± 0.05	17.58	9.98	1.600	1.592	−2.108	465.3 ± 2.1	6.13 ± 0.04
Z1738	Cu	14.98 ± 0.05	17.80	10.14	1.600	1.594	−2.059	478.4 ± 2.1	6.16 ± 0.04
Z1955	Al	20.38 ± 0.06	17.98	10.36	1.600	1.701	−3.326	493.8 ± 2.1	6.25 ± 0.04
Z1956	Al	20.40 ± 0.05	18.00	10.37	1.600	1.263	−3.428	494.8 ± 1.8	6.25 ± 0.04
Z1918	Cu	15.20 ± 0.05	18.04	10.28	1.600	1.603	−2.057	491.3 ± 2.1	6.16 ± 0.04
Z1911	Al	20.58 ± 0.05	18.20	10.45	1.600	1.258	−3.395	503.8 ± 1.8	6.22 ± 0.04
Z1911	Al	20.61 ± 0.05	18.20	10.46	1.600	1.258	−3.399	504.4 ± 1.8	6.23 ± 0.04
Z1911	Al	20.59 ± 0.05	18.20	10.44	1.600	1.251	−3.378	503.5 ± 1.8	6.22 ± 0.04
Z1909	Al	20.70 ± 0.05	18.29	10.50	1.600	1.253	−3.348	508.7 ± 1.9	6.22 ± 0.04
Z1918	Cu	15.45 ± 0.05	18.29	10.44	1.600	1.610	−2.081	505.9 ± 2.2	6.18 ± 0.04
Z1909	Al	20.80 ± 0.05	18.32	10.56	1.600	1.258	−3.398	512.3 ± 1.9	6.26 ± 0.04
Z1909	Al	20.80 ± 0.05	18.32	10.56	1.600	1.255	−3.299	512.3 ± 1.9	6.26 ± 0.04
Z2025	Al	20.84 ± 0.05	18.35	10.57	1.600	1.257	−3.398	514.1 ± 1.9	6.26 ± 0.04
Z2045	Al	20.94 ± 0.05	18.38	10.63	1.600	1.255	−3.445	517.7 ± 1.9	6.29 ± 0.04
Z2045	Al	20.93 ± 0.05	18.41	10.62	1.600	1.252	−3.440	517.9 ± 1.9	6.26 ± 0.04
Z2187	Cu	15.73 ± 0.05	18.56	10.62	1.600	1.603	−2.081	522.2 ± 2.2	6.20 ± 0.04
Z1972	Al	21.38 ± 0.06	18.62	10.86	2.500	1.724	−5.351	535.6 ± 2.2	6.36 ± 0.05
Z2125	Al	21.27 ± 0.05	18.63	10.79	1.600	1.246	−3.415	532.4 ± 1.9	6.30 ± 0.04
Z1742	Cu	15.83 ± 0.05	18.64	10.69	1.600	1.600	−2.106	527.8 ± 2.2	6.21 ± 0.04
Z1972	Al	21.52 ± 0.06	18.76	10.92	2.500	1.729	−5.434	542.6 ± 2.2	6.34 ± 0.05
Z1988	Al	21.63 ± 0.05	18.83	10.97	1.600	1.248	−3.445	547.3 ± 1.9	6.35 ± 0.04
Z1742	Cu	16.27 ± 0.05	18.86	11.00	1.600	1.623	−2.025	549.5 ± 2.3	6.36 ± 0.04
Z2112	Cu	16.12 ± 0.05	18.88	10.88	1.600	1.625	−2.112	544.2 ± 2.3	6.26 ± 0.04
Z1955	Al	21.84 ± 0.06	18.98	11.07	1.600	1.703	−3.366	556.7 ± 2.2	6.36 ± 0.04
Z1917	Cu	16.34 ± 0.05	18.99	11.03	1.600	1.622	−2.163	555.2 ± 2.3	6.33 ± 0.04
Z1406	Al	21.80 ± 0.15	19.01	11.04	36.000	10.743	−77.820	556.0 ± 5.9	6.33 ± 0.14
Z1917	Cu	16.30 ± 0.05	19.04	11.00	1.600	1.635	−2.059	554.8 ± 2.3	6.27 ± 0.04
Z1406	Al	22.30 ± 0.15	19.17	11.32	36.600	10.987	−79.525	575.0 ± 6.1	6.48 ± 0.15
Z1956	Al	22.25 ± 0.05	19.23	11.28	1.600	1.264	−3.362	574.5 ± 2.0	6.41 ± 0.04
Z1911	Al	22.20 ± 0.05	19.30	11.23	1.600	1.257	−3.415	574.3 ± 2.0	6.34 ± 0.04
Z1911	Al	22.20 ± 0.05	19.32	11.23	1.600	1.266	−3.534	574.6 ± 2.0	6.33 ± 0.04
Z1911	Al	22.20 ± 0.05	19.32	11.23	1.600	1.263	−3.374	574.6 ± 2.0	6.33 ± 0.04
Z1909	Al	22.30 ± 0.05	19.34	11.28	1.600	1.261	−3.522	578.2 ± 2.0	6.36 ± 0.04

TABLE X. (*Continued.*)

Expt.	Flyer	v_f (km/s)	U_s^{quartz} (km/s)	u_p^{quartz} (km/s)	$\sigma_{U_s}^2$ ($\times 10^{-3}$)	$\sigma_{u_p}^2$ ($\times 10^{-3}$)	$\sigma_{U_s}\sigma_{u_p}$ ($\times 10^{-4}$)	P (GPa)	ρ (g/cc)
Z1201	Al	22.60 ± 0.15	19.42	11.46	37.600	10.956	−81.353	589.5 ± 6.2	6.47 ± 0.15
Z1909	Al	22.40 ± 0.05	19.44	11.33	1.600	1.259	−3.448	583.4 ± 2.0	6.35 ± 0.04
Z1909	Al	22.40 ± 0.05	19.44	11.33	1.600	1.268	−3.487	583.4 ± 2.0	6.35 ± 0.04
Z2037	Al	22.60 ± 0.05	19.49	11.44	1.600	1.258	−3.429	590.9 ± 2.0	6.42 ± 0.04
Z2037	Al	22.69 ± 0.05	19.52	11.49	1.600	1.266	−3.515	594.4 ± 2.0	6.44 ± 0.04
Z1740	Cu	17.16 ± 0.05	19.69	11.65	3.600	4.387	−7.957	607.9 ± 3.6	6.49 ± 0.07
Z1807	Al	23.00 ± 0.10	19.69	11.57	1.600	1.639	−2.104	603.8 ± 2.4	6.43 ± 0.04
Z2148	Al	23.00 ± 0.05	19.75	11.64	1.600	1.264	−3.330	609.1 ± 2.0	6.45 ± 0.04
Z2147	Al	23.05 ± 0.05	19.77	11.67	1.600	1.277	−3.514	611.1 ± 2.0	6.47 ± 0.04
Z1742	Cu	17.07 ± 0.05	19.81	11.49	1.600	1.643	−2.111	603.0 ± 2.4	6.31 ± 0.04
Z1806	Al	23.40 ± 0.15	19.89	11.86	10.000	9.738	−22.197	625.1 ± 5.5	6.57 ± 0.10
Z1742	Cu	17.50 ± 0.05	20.14	11.96	1.600	1.283	−3.469	638.5 ± 2.1	6.53 ± 0.04
Z2125	Al	23.65 ± 0.05	20.14	11.78	1.600	1.645	−2.165	628.5 ± 2.5	6.38 ± 0.04
Z1743	Cu	17.75 ± 0.05	20.16	11.97	1.600	1.677	−2.202	639.3 ± 2.5	6.52 ± 0.04
Z1988	Al	23.69 ± 0.05	20.17	11.98	1.600	1.292	−3.510	640.5 ± 2.1	6.53 ± 0.04
Z1740	Cu	17.60 ± 0.05	20.19	11.85	1.600	1.654	−2.158	633.8 ± 2.5	6.41 ± 0.04
Z1917	Cu	17.60 ± 0.05	20.24	11.84	1.600	1.674	−2.217	635.0 ± 2.5	6.39 ± 0.04
Z1917	Cu	17.60 ± 0.05	20.24	11.84	1.600	1.654	−2.102	635.0 ± 2.5	6.39 ± 0.04
Z1988	Al	23.77 ± 0.05	20.27	12.01	1.600	1.297	−3.581	645.2 ± 2.1	6.51 ± 0.04
Z1881	Al	23.85 ± 0.10	20.31	12.05	3.600	4.421	−7.987	648.7 ± 3.7	6.52 ± 0.06
Z1452	Al	23.85 ± 0.14	20.34	12.05	10.000	8.544	−22.222	649.4 ± 5.3	6.50 ± 0.10
Z1912	Al	24.12 ± 0.05	20.52	12.18	1.600	1.295	−3.449	662.3 ± 2.1	6.52 ± 0.04
Z1912	Al	24.28 ± 0.05	20.56	12.30	1.600	1.299	−3.541	670.0 ± 2.1	6.59 ± 0.04
Z2044	Al	24.32 ± 0.05	20.56	12.27	1.600	1.306	−3.559	668.6 ± 2.1	6.57 ± 0.04
Z1743	Cu	18.07 ± 0.05	20.57	12.16	1.600	1.688	−2.167	662.7 ± 2.5	6.48 ± 0.04
Z2044	Al	24.35 ± 0.05	20.61	12.31	1.600	1.309	−3.649	672.1 ± 2.1	6.58 ± 0.04
Z1910	Al	24.40 ± 0.05	20.69	12.29	1.600	1.298	−3.495	673.7 ± 2.1	6.53 ± 0.04
Z1910	Al	24.40 ± 0.05	20.69	12.32	1.600	1.302	−3.492	675.4 ± 2.2	6.55 ± 0.04
Z1910	Al	24.35 ± 0.05	20.69	12.32	1.600	1.307	−3.517	675.5 ± 2.2	6.55 ± 0.04
Z2148	Al	24.59 ± 0.05	20.72	12.43	1.600	1.311	−3.519	682.7 ± 2.2	6.63 ± 0.04
Z1957	Al	24.66 ± 0.06	20.75	12.47	1.600	1.760	−3.545	685.8 ± 2.5	6.64 ± 0.04
Z2094	Al	24.60 ± 0.05	20.75	12.43	1.600	1.316	−3.565	683.7 ± 2.2	6.61 ± 0.04
Z1806	Al	24.85 ± 0.15	20.99	12.54	10.000	9.726	−21.725	697.5 ± 5.8	6.58 ± 0.10
Z1881	Al	25.10 ± 0.10	21.24	12.64	3.600	4.410	−7.613	711.6 ± 3.9	6.55 ± 0.06
Z1881	Al	25.25 ± 0.10	21.29	12.73	3.600	4.438	−7.867	718.1 ± 3.9	6.59 ± 0.06
Z1136	Al	25.40 ± 0.25	21.34	12.81	45.400	28.438	−98.803	724.5 ± 10.3	6.64 ± 0.19
Z1912	Al	25.60 ± 0.05	21.54	12.94	1.600	1.370	−3.468	738.6 ± 2.3	6.64 ± 0.04
Z1912	Al	25.67 ± 0.05	21.54	12.89	1.600	1.352	−3.554	736.0 ± 2.3	6.60 ± 0.04
Z1912	Al	25.66 ± 0.05	21.59	12.92	1.600	1.355	−3.480	739.3 ± 2.3	6.60 ± 0.04
Z2345	Al	26.02 ± 0.05	21.65	13.14	1.600	1.380	−3.589	753.7 ± 2.3	6.74 ± 0.04
Z1910	Al	25.90 ± 0.05	21.69	13.19	1.600	1.824	−3.499	758.2 ± 2.6	6.76 ± 0.04
Z1957	Al	26.12 ± 0.06	21.69	13.05	1.600	1.370	−3.487	750.2 ± 2.3	6.65 ± 0.04
Z2333	Al	26.00 ± 0.05	21.69	13.11	1.600	1.370	−3.571	753.8 ± 2.3	6.70 ± 0.04
Z1472	Al	26.08 ± 0.14	21.70	13.16	10.000	8.704	−21.970	757.0 ± 5.7	6.74 ± 0.10
Z1910	Al	25.95 ± 0.05	21.74	13.07	1.600	1.361	−3.488	753.1 ± 2.3	6.65 ± 0.04
Z1910	Al	26.01 ± 0.05	21.79	13.10	1.600	1.368	−3.420	756.4 ± 2.3	6.64 ± 0.04
Z2165	Al	26.20 ± 0.05	21.84	13.21	1.600	1.385	−3.606	764.5 ± 2.3	6.70 ± 0.04
Z1889	Al	26.24 ± 0.10	21.86	13.23	3.600	4.496	−7.868	766.4 ± 4.1	6.71 ± 0.06
Z1474	Al	26.30 ± 0.14	21.90	13.26	10.000	8.771	−22.881	769.5 ± 5.7	6.72 ± 0.10
Z1991	Al	26.52 ± 0.05	21.98	13.38	1.600	1.406	−3.455	779.4 ± 2.4	6.77 ± 0.04
Z1474	Al	26.60 ± 0.14	22.01	13.42	10.000	8.728	−22.059	783.1 ± 5.8	6.79 ± 0.10
Z2094	Al	26.75 ± 0.05	22.09	13.50	1.600	1.422	−3.543	790.4 ± 2.4	6.81 ± 0.04
Z1882	Al	26.70 ± 0.10	22.14	13.46	3.600	4.541	−8.149	789.8 ± 4.2	6.76 ± 0.06
Z1989	Al	26.78 ± 0.05	22.17	13.50	1.600	1.421	−3.654	793.4 ± 2.4	6.78 ± 0.04
Z1472	Al	26.92 ± 0.14	22.19	13.59	10.000	8.736	−22.703	799.1 ± 5.8	6.84 ± 0.10
Z1239	Al	26.80 ± 0.27	22.28	13.49	49.500	31.620	−111.118	796.7 ± 11.3	6.73 ± 0.19
Z2043	Al	27.12 ± 0.05	22.30	13.69	1.600	1.442	−3.588	809.1 ± 2.5	6.86 ± 0.04
Z2043	Al	27.12 ± 0.05	22.33	13.68	1.600	1.434	−3.521	809.8 ± 2.5	6.84 ± 0.04
Z1882	Al	27.00 ± 0.10	22.34	13.60	3.600	4.555	−7.788	805.6 ± 4.2	6.78 ± 0.06

TABLE X. (*Continued.*)

Expt.	Flyer	v_f (km/s)	U_s^{quartz} (km/s)	u_p^{quartz} (km/s)	$\sigma^2_{U_s}$ ($\times 10^{-3}$)	$\sigma^2_{u_p}$ ($\times 10^{-3}$)	$\sigma_{U_s}\sigma_{u_p}$ ($\times 10^{-4}$)	P (GPa)	ρ (g/cc)
Z1238	Al	27.20 ± 0.27	22.38	13.72	49.900	32.858	−108.655	814.0 ± 11.6	6.86 ± 0.20
Z1958	Al	27.15 ± 0.05	22.39	13.69	1.600	1.433	−3.475	812.3 ± 2.5	6.82 ± 0.04
Z1350	Al	27.80 ± 0.15	22.57	14.06	50.800	12.189	−114.753	841.2 ± 8.0	7.04 ± 0.18
Z1985	Cu	20.35 ± 0.20	22.58	13.65	10.000	24.456	−13.496	816.8 ± 9.8	6.70 ± 0.13
Z2333	Al	27.70 ± 0.05	22.75	13.96	1.600	1.471	−3.561	841.7 ± 2.5	6.86 ± 0.04
Z1473	Al	27.90 ± 0.14	22.84	14.07	10.000	8.857	−22.742	851.5 ± 6.1	6.90 ± 0.10
Z2165	Al	27.93 ± 0.05	22.87	14.08	1.600	1.500	−3.621	853.4 ± 2.6	6.89 ± 0.04
Z1989	Al	28.25 ± 0.05	23.02	14.25	1.600	1.527	−3.556	869.3 ± 2.6	6.95 ± 0.04
Z1424	Al	28.40 ± 0.14	23.04	14.08	10.000	8.829	−22.945	860.1 ± 6.1	6.82 ± 0.09
Z1473	Al	28.00 ± 0.14	23.04	14.34	10.000	8.902	−22.280	875.7 ± 6.1	7.02 ± 0.10
Z1985	Cu	21.00 ± 0.20	23.07	14.08	10.000	24.552	−13.558	861.2 ± 10.0	6.80 ± 0.13
Z1424	Al	28.80 ± 0.14	23.14	14.57	10.000	8.953	−23.174	893.7 ± 6.2	7.16 ± 0.10
Z1989	Al	28.50 ± 0.05	23.15	14.38	1.600	1.550	−3.649	882.2 ± 2.6	6.99 ± 0.04
Z1882	Al	28.40 ± 0.10	23.19	14.31	3.600	4.673	−8.175	879.3 ± 4.4	6.92 ± 0.07
Z1350	Al	28.80 ± 0.15	23.29	14.54	54.000	12.458	−122.840	897.2 ± 8.4	7.06 ± 0.18
Z1958	Al	28.70 ± 0.05	23.40	14.45	1.600	1.550	−3.513	895.9 ± 2.7	6.93 ± 0.04
Z1949	Al	29.05 ± 0.10	23.47	14.66	4.900	4.814	−11.292	911.5 ± 4.6	7.06 ± 0.07
Z2018	Al	28.95 ± 0.07	23.50	14.59	1.600	2.552	−3.517	908.3 ± 3.3	6.99 ± 0.05
Z1959	Al	29.27 ± 0.06	23.51	14.79	1.600	2.041	−3.661	921.3 ± 3.0	7.15 ± 0.05
Z2166	Al	28.89 ± 0.05	23.51	14.55	1.600	1.589	−3.646	906.2 ± 2.7	6.95 ± 0.04
Z2018	Al	29.05 ± 0.07	23.53	14.65	1.600	2.573	−3.649	913.0 ± 3.3	7.02 ± 0.05
Z2371	Al	29.56 ± 0.05	23.93	14.88	1.600	1.636	−3.655	943.4 ± 2.8	7.01 ± 0.04
Z2166	Al	30.45 ± 0.05	24.42	15.34	1.600	1.719	−3.675	992.3 ± 2.9	7.13 ± 0.04
Z1810	Al	30.47 ± 0.05	24.45	15.28	1.600	1.828	−8.328	990.2 ± 3.1	7.07 ± 0.05
Z1928	Al	30.38 ± 0.05	24.45	15.34	3.600	1.719	−3.654	994.0 ± 2.9	7.12 ± 0.04
Z1959	Al	30.68 ± 0.05	24.47	15.47	1.600	1.739	−3.633	1003.2 ± 2.9	7.21 ± 0.04
Z2015	Al	31.33 ± 0.05	24.90	15.79	1.600	1.812	−3.641	1041.7 ± 3.1	7.24 ± 0.04
Z2375	Al	31.24 ± 0.05	24.95	15.72	1.600	1.816	−3.625	1039.3 ± 3.1	7.16 ± 0.04
Z2375	Al	31.25 ± 0.05	25.05	15.70	1.600	1.809	−3.717	1042.4 ± 3.1	7.10 ± 0.04
Z1948	Al	31.95 ± 0.10	25.25	16.11	4.900	5.117	−11.062	1077.6 ± 5.1	7.32 ± 0.07
Z2016	Al	32.50 ± 0.05	25.60	16.38	1.600	1.955	−3.728	1111.0 ± 3.2	7.36 ± 0.04
Z2332	Al	32.50 ± 0.05	25.60	16.38	1.600	1.955	−3.616	1111.0 ± 3.3	7.36 ± 0.04
Z1367	Al	33.00 ± 0.20	26.05	16.59	67.600	20.818	−153.608	1145.4 ± 11.7	7.31 ± 0.20
Z1929	Al	33.50 ± 0.05	26.18	16.88	2.500	2.161	−5.926	1171.3 ± 3.5	7.46 ± 0.05
Z1929	Al	33.50 ± 0.05	26.25	16.87	2.500	2.149	−5.693	1173.3 ± 3.6	7.41 ± 0.05
Z1419	Al	33.80 ± 0.14	26.35	17.04	10.000	9.728	−23.432	1189.6 ± 7.3	7.50 ± 0.10
Z1929	Al	33.80 ± 0.05	26.35	17.04	1.600	2.160	−3.703	1189.6 ± 3.5	7.50 ± 0.05
Z1490	Al	33.85 ± 0.14	26.49	17.04	10.000	9.657	−23.378	1196.0 ± 7.4	7.43 ± 0.10
Z1929	Al	34.00 ± 0.05	26.55	17.12	10.000	2.619	−22.924	1204.4 ± 4.5	7.46 ± 0.08
Z1932	Al	34.45 ± 0.05	26.95	17.35	2.500	2.730	−23.336	1238.8 ± 4.6	7.44 ± 0.08
Z1929	Al	34.50 ± 0.05	26.95	17.31	10.000	2.302	−5.806	1236.6 ± 3.8	7.41 ± 0.05
Z1932	Al	34.80 ± 0.05	27.15	17.49	2.500	2.350	−5.746	1258.6 ± 3.8	7.45 ± 0.05
Z1932	Al	35.40 ± 0.05	27.55	17.78	2.500	2.455	−5.895	1298.4 ± 4.0	7.47 ± 0.05
Z1933	Al	38.20 ± 0.08	29.36	19.16	4.900	4.764	−11.134	1490.5 ± 5.8	7.63 ± 0.07
Z1933	Al	39.50 ± 0.08	29.96	19.85	4.900	5.009	−11.171	1576.2 ± 6.1	7.86 ± 0.07

TABLE XI. Aluminum (Refs. 6,9–12,14,15,51–55) and copper (Refs. 6,12,51,53,55–58) $U_s - u_p$ coefficients and covariance matrix elements. Break points between the low- and high-pressure branches of the Hugoniots are $u_p = 6.25$ and 4.27 km/s for aluminum and copper, respectively.

	C_0 (km/s)	S	$\sigma^2_{C_0}$ ($\times 10^{-3}$)	σ^2_S ($\times 10^{-3}$)	$\sigma_{C_0}\sigma_S$ ($\times 10^{-3}$)
Low-P Al	5.385	1.339	0.3141	0.1097	−0.1576
High-P Al	6.322	1.189	53.581	0.4196	−4.605
Low-P Cu	3.970	1.479	0.2925	0.5002	0.3792
High-P Cu	4.384	1.382	13.44	0.6084	−2.689

TABLE XII. α-quartz coefficients for the $U_s - u_p$ relation displayed in Eq. (A1).

a (km/s)	b	c	d $(\text{km/s})^{-1}$
6.278	1.193	2.505	0.3701

TABLE XIII. α-quartz covariance matrix elements for the $U_s - u_p$ relation displayed in Eq. (A1).

σ_a^2 $(\times 10^{-2})$	$\sigma_a\sigma_b$ $(\times 10^{-3})$	$\sigma_a\sigma_c$ $(\times 10^{-3})$	$\sigma_a\sigma_d$ $(\times 10^{-3})$	σ_b^2 $(\times 10^{-4})$	$\sigma_b\sigma_c$ $(\times 10^{-4})$	$\sigma_b\sigma_d$ $(\times 10^{-4})$	σ_c^2 $(\times 10^{-3})$	$\sigma_c\sigma_d$ $(\times 10^{-4})$	σ_d^2 $(\times 10^{-4})$
4.247	−2.428	4.492	−2.727	1.401	−3.202	1.506	7.594	1.705	2.080

*mdknuds@sandia.gov

[1] T. Guillot, Science **286**, 72 (1999).
[2] I. Baraffe, G. Chabrier, and T. Barman, Astron. Astrophys. **482**, 315 (2008).
[3] J. Fortney and N. Nettelmann, Space Sci. Rev. **152**, 423 (2009).
[4] J. Lindl, *Inertial Confinement Fusion* (Springer, New York, 1998).
[5] J. Lindl, Phys. Plasmas **2**, 3933 (1995).
[6] A. C. Mitchell and W. J. Nellis, J. Appl. Phys. **52**, 3363 (1981).
[7] L. V. Al'tshuler, K. K. Krupnikov, B. N. Ledenev, V. I. Zhuckikhin, and M. I. Brazhnik, Zh. Eksp. Teor. Fiz. **34**, 874 (1958) [Sov. Phys.–JETP **7**, 606 (1958)].
[8] R. G. McQueen, S. P. Marsh, J. W. Taylor, N. Fritz, and W. J. Carter, *High Velocity Impact Phenomena* (Academic, New York, 1970), p. 515.
[9] L. V. Al'tshuler, S. B. Kormer, A. A. Bakanova, and R. F. Trunin, Zh. Eksp. Teor. Fiz. **38**, 790 (1960) [Sov. Phys.–JETP **11**, 573 (1960)].
[10] B. L. Glushk, A. P. Zharkov, M. V. Zhernokletov, V. Y. Ternovoi, A. S. Filimonov, and V. E. Fortov, Zh. Eksp. Teor. Fiz. **96**, 1301 (1989) [Sov. Phys.–JETP **69**, 739 (1989)].
[11] M. D. Knudson, R. W. Lemke, D. B. Hayes, C. A. Hall, C. Deeney, and J. R. Asay, J. Appl. Phys. **94**, 4420 (2003).
[12] A. C. Mitchell, W. J. Nellis, J. A. Moriarty, R. A. Heinle, N. C. Holmes, R. E. Tipton, and G. W. Repp, J. Appl. Phys. **69**, 2981 (1991); a reanalysis of the Cu data was performed to correct for a too stiff aluminum standard.
[13] L. V. Al'tshuler, A. A. Bakanova, I. P. Dudoladov, E. A. Dynin, R. F. Trunin, and B. S. Chekin, J. Appl. Mech. Tech. Phys. **22**, 145 (1981).
[14] L. P. Volkov, N. P. Voloshin, A. S. Vladimirov, V. N. Nogin, and V. A. Simonenko, Pis'ma Zh. Eksp. Teor. Fiz. **31**, 623 (1980) [JETP Lett. **31**, 588 (1980)].
[15] V. A. Simonenko, N. P. Voloshin, A. S. Vladimirov, A. P. Nagibin, V. N. Nogin, V. A. Popov, V. A. Sal'nikov, and Y. A. Shoidin, Zh. Eksp. Teor. Fiz. **88**, 1452 (1985) [Sov. Phys.–JETP **61**, 869 (1985)].
[16] C. E. Ragan, Phys. Rev. A **25**, 3360 (1982).
[17] C. E. Ragan, Phys. Rev. A **29**, 1391 (1984).
[18] D. G. Hicks, T. R. Boehly, P. M. Celliers, J. H. Eggert, E. Vianello, D. D. Meyerhofer, and G. W. Collins, Phys. Plasmas **12**, 082702 (2005).
[19] M. D. Knudson and M. P. Desjarlais, Phys. Rev. Lett. **103**, 225501 (2009); see also the Appendix.
[20] D. G. Hicks, T. R. Boehly, J. H. Eggert, J. E. Miller, P. M. Celliers, and G. W. Collins, Phys. Rev. Lett. **97**, 025502 (2006).
[21] L. M. Barker and R. E. Hollenbach, J. Appl. Phys. **43**, 4669 (1972).
[22] S. Root, K. R. Cochrane, J. H. Carpenter, and T. R. Mattsson, Phys. Rev. B **87**, 224102 (2013).
[23] M. A. Barrios, T. R. Boehly, D. G. Hicks, D. E. Fratanduono, J. H. Eggert, G. W. Collins, and D. D. Meyerhofer, J. Appl. Phys. **111**, 093515 (2012).
[24] S. Root, R. J. Magyar, J. H. Carpenter, D. L. Hanson, and T. R. Mattsson, Phys. Rev. Lett. **105**, 085501 (2010).
[25] M. D. Knudson, M. P. Desjarlais, R. W. Lemke, T. R. Mattsson, M. French, N. Nettelmann, and R. Redmer, Phys. Rev. Lett. **108**, 091102 (2012).
[26] J. H. Eggert, S. Brygoo, P. Loubeyre, R. S. McWilliams, P. M. Celliers, D. G. Hicks, T. R. Boehly, R. Jeanloz, and G. W. Collins, Phys. Rev. Lett. **100**, 124503 (2008).
[27] D. G. Hicks, T. R. Boehly, P. M. Celliers, J. H. Eggert, S. J. Moon, D. D. Meyerhofer, and G. W. Collins, Phys. Rev. B **79**, 014112 (2009).
[28] P. Loubeyre, S. Brygoo, J. Eggert, P. M. Celliers, D. K. Spaulding, J. R. Rygg, T. R. Boehly, G. W. Collins, and R. Jeanloz, Phys. Rev. B **86**, 144115 (2012).
[29] G. E. Duvall and R. A. Graham, Rev. Mod. Phys. **49**, 523 (1977).
[30] M. D. Knudson, J. R. Asay, and C. Deeney, J. Appl. Phys. **97**, 073514 (2005).
[31] R. Hemley, C. Prewitt, and K. Kingma, Rev. Mineral. **29**, 41 (1994).
[32] C. Agnor, R. Canup, and H. Levison, Icarus **142**, 219 (1999).
[33] M. D. Knudson and R. W. Lemke J. Appl. Phys. (to be published).
[34] S. Root (unpublished).
[35] G. Kresse and J. Furthmüller, Phys. Rev. B **54**, 11169 (1996).
[36] P. E. Blöchl, Phys. Rev. B **50**, 17953 (1994).
[37] G. Kresse and D. Joubert, Phys. Rev. B **59**, 1758 (1999).
[38] R. Armiento and A. E. Mattsson, Phys. Rev. B **72**, 085108 (2005).
[39] D. G. Hicks, T. R. Boehly, P. M. Celliers, D. K. Bradley, J. H. Eggert, R. S. McWilliams, R. Jeanloz, and G. W. Collins, Phys. Rev. B **78**, 174102 (2008).
[40] R. F. Trunin, *Shock Compression of Condensed Materials* (Cambridge University Press, Cambridge, England, 1998), p. 763.
[41] R. F. Trunin, Phys. Usp. **37**, 1123 (1994).
[42] M. Matzen *et al.*, Phys. Plasmas **12**, 055503 (2005).
[43] R. Lemke, M. D. Knudson, A. Robinson, T. Haill, K. Struve, J. Asay, and T. Mehlhorn, Phys. Plasmas **10**, 1867 (2003).
[44] R. Lemke, M. D. Knudson, and J.-P. Davis, Int. J. Impact Eng. **38**, 480 (2011).
[45] G. G. Ghosh, Opt. Commun. **163**, 95 (1999).

[46]From manufacturers website: http://www.mitsuichemicals.com/tpx.htm

[47]A. F. Danilyuk, V. L. Kirillov, M. D. Savelieva, V. S. Bobrovnikov, A. R. Buzykaev, E. A. Kravchenko, A. V. Lavrov, and A. P. Onuchin, Nucl. Instrum. Methods Phys. Res., Sect. A **494**, 491 (2002).

[48]D. Richter and D. Lipka, Nucl. Instrum. Methods Phys. Res., Sect. A **513**, 635 (2003).

[49]J. Taylor, *An Introduction to Error Analysis, The Study of Uncertainties in Physical Measurements* (University Science Books, Sausalito, CA, 1982).

[50]S. Hamel, L. X. Benedict, P. M. Celliers, M. A. Barrios, T. R. Boehly, G. W. Collins, T. Döppner, J. H. Eggert, D. R. Farley, D. G. Hicks, J. L. Kline, A. Lazicki, S. LePape, A. J. Mackinnon, J. D. Moody, H. F. Robey, E. Schwegler, and P. A. Sterne, Phys. Rev. B **86**, 094113 (2012).

[51]*LASL Shock Hugoniot Data*, edited by S. P. Marsh (University of California Press, Berkeley, CA, 1980).

[52]S. B. Kormer, A. I. Funtikov, V. D. Urlin, and A. N. Kolesnikova, Zh. Eksp. Teor. Fiz. **42**, 626 (1962) [Sov. Phys.–JETP **15**, 477 (1962)].

[53]L. V. Al'tshuler, N. N. Kalitkin, L. V. Kuz'mina, and B. S. Chekin, Zh. Eksp. Teor. Fiz. **72**, 317 (1977) [Sov. Phys.–JETP **45**, 167 (1977)].

[54]R. H. Warnes, J. Chem. Phys. **53**, 1088 (1970).

[55]M. D. Knudson (unpublished).

[56]W. H. Isbell, F. H. Shipman, and A. H. Jones, General Motors Corporation Report No. MSL-68-13, 1968.

[57]D. Hayes, R. S. Hixson, and R. G. McQueen, *Shock Compression of Condensed Matter–1999* (AIP, New York, 2000), p. 483.

[58]L. V. Al'tshuler, A. A. Bakanova, and R. F. Trunin, Zh. Eksp. Teor. Fiz. **42**, 91 (1962) [Sov. Phys.–JETP **15**, 65 (1962)].